

Supplementary Materials for

Local Connectivity and Synaptic Dynamics in Mouse and Human Neocortex

Luke Campagnola, Stephanie C Seeman, Thomas Chartrand, Lisa Kim, Alex Hoggarth, Clare Gamlin, Shinya Ito, Jessica Trinh, Pasha Davoudian, Cristina Radaelli, Mean-Hwan Kim, Travis Hage, Thomas Braun, Lauren Alfiler, Julia Andrade, Phillip Bohn, Rachel Dalley, Alex Henry, Sara Kebede, Alice, Mukora, David Sandman, Grace Williams, Rachael Larsen, Corinne Teeter, Tanya L. Daigle¹, Kyla Berry, Nadia Dotson, Rachel Enstrom, Melissa Gorham, Madie Hupp, Samuel Dingman Lee, Kiet Ngo, Philip R Nicovich, Lydia Potekhina, Shea Ransford, Amanda Gary, Jeff Goldy, Delissa McMillen, Trangthanh Pham, Michael Tieu, La'Akea Siverts, Miranda Walker, Colin Farrell, Martin Schroedter, Cliff Slaughterbeck, Charles Cobb, Richard Ellenbogen, Ryder P Gwinn, C. Dirk Keene, Andrew L Ko, Jeffrey G Ojemann, Daniel L Silbergeld, Daniel Carey, Tamara Casper, Kirsten Crichton, Michael Clark, Nick Dee, Lauren Ellingwood¹, Jessica Gloe¹, Matthew Kroll¹, Josef Sulc¹, Herman Tung¹, Katherine Wadhvani, Krissy Brouner, Tom Egdorf, Michelle Maxwell, Medea McGraw, Christina Alice Pom, Augustin Ruiz, Jasmine Bomben, David Feng, Nika Hejazinia, Shu Shi, Aaron Szafer, Wayne Wakeman, John Phillips, Amy Bernard, Luke Esposito, Florence D D'Orazi, Susan Sunkin, Kimberly Smith, Bosiljka Tasic, Anton Arkhipov, Staci Sorensen, Ed Lein, Christof Koch, Gabe Murphy, Hongkui Zeng, Tim Jarsky

Correspondence to: timj@alleninstitute.org

This file includes:

Materials and Methods
Figs. S1 to S14
Tables S1 to S5

Materials and Methods

Methods were similar to Seeman, Campagnola et. al, 2018. Information on the Synaptic Physiology pipeline and the dataset are accessible from our website (Synaptic Physiology Coarse Matrix Dataset). Statistical tests are abbreviated as follows: Mann-Whitney U test (MW), Kolmogorov Smirnov test (KS), Kruskal-Wallis one-way analysis of variance (KW). Full Standard Operating Procedures can be found: <https://www.protocols.io/workspaces/allen-institute-for-brain-science/publications?categories=multipatch>

Animals and tissue preparation

All animal procedures were approved by the Institutional Animal Care and Use Committee at the Allen Institute for Brain Science (Seattle, WA), which operates per National Institutes of Health guidelines. Triple (T.L.D., unpublished) and quadruple (24) mouse lines generated using double transgenic mouse lines, were used to target up to two unique cell subclasses in a single animal (see Table S1, <http://portal.brain-map.org/explore/toolkit/mice>). Each subclass was selectively labeled by fluorescent reporters (tdTomato or EGFP) driven by Cre or FlpO. Layer-specific excitatory cells were targeted using unique transgenic drivers: Nr5a1 and Rorb for layer 4, Sim1, and Tlx3 for layer 5 ET and IT, respectively, and Ntsr1 for layer 6 CT. It was generally not possible to generate crosses of two excitatory drivers, however in L5 we were able to target ET cells via a retroorbital injection of mscRE4-FlpO AAV PHPe.B (75) into Tlx3-Cre transgenic mice in order to probe interconnections of L5 ET and IT cells. Transgenic lines were not used to target layer 2/3 excitatory cells but were later confirmed through the presence of dendritic spines via post-hoc morphological analysis (see Morphology and Position). Inhibitory cell subclasses, Sst, Pvalb, and Vip, were targeted in all layers.

Female and male adult mice (mean age 46.0 ± 4.6 ; SD) were anesthetized with 5% isoflurane and transcardially perfused with ice-cold oxygenated slicing aCSF I. All aCSF recipes are in Table S3.

Acute parasagittal slices (350 μ m) were produced with a Compressstome (Precisionary Instruments) or VT1200S Vibratome (Leica Biosystems) in ice-cold aCSF I solution. The slicing angle was set to 17° relative to the sagittal plane to preserve pyramidal cells' apical dendrites. Slices were then recovered for 10 min in a holding chamber containing oxygenated aCSF I maintained at 34°C. After recovery, slices were kept in room temperature oxygenated aCSF IV (Table S3).

Human neocortical tissue from Temporal, Frontal, and Parietal lobes was obtained from adult patients undergoing neurosurgery for the treatment of epilepsy (52 samples) or tumor (20 samples; Fig 1A). Tissue obtained from surgery was distal to the core pathological tissue and was deemed not to be of diagnostic value. Surgical specimens were placed in a sterile container filled with pre-chilled (2-4°C), carbogenated aCSF VII containing decreased sodium replaced with NMDG to reduce oxidative damage (Table S3), and delivered from the surgical site to the laboratory within 10-40 min.

In the laboratory, specimens were trimmed to isolate regions of interest and mounted to preserve intact cortical columns (pial surface to white matter) before being sliced in aCSF VII using a Compressstome or Vibratome. Slices were then transferred to oxygenated aCSF VII (34°C) for 10 min, then moved and kept in aCSF VIII at room temperature (Table S3) for a minimum of one hour prior to recording.

Electrophysiological recordings

Slices were placed in custom recording chambers perfused (2-4 mL/min) with aCSF IX which contained one of two external calcium concentrations ($[Ca^{++}]_e$) 1.3 mM or 2.0 mM (Table S3). aCSF IX in the recording chamber was measured at 31-33°C, pH 7.2-7.3, and 30-50% oxygen saturation. In our previous study (13), we conducted experiments in mouse with a $[Ca^{++}]_e$ of 2 mM to be consistent with previous connectivity studies (6, 26, 76, 77). However, external calcium concentration *in vivo* has been measured to be closer to 1 mM (78) and more closely reproduces *in vivo*-like short term plasticity *in vitro* (79). Thus, we reduced $[Ca^{++}]_e$ to 1.3 mM to measure synaptic properties closer to physiological conditions. However, when we compared connection probability, strength, and short-term plasticity for connection elements in which we had data at both $[Ca^{++}]_e$ (21 elements for connectivity and 10 elements for synaptic properties out of 89 targeted intralaminar elements), we found connectivity and connection characteristics were consistent between the two concentrations (Fig S8). Thus for results reported in this study, data were pooled across conditions. Experiments on human tissue were conducted with 1.3 mM $[Ca^{++}]_e$ only.

Recording pipettes (Sutter Instruments) were pulled using a DMZ Zeitz-Puller (Zeitz) to a tip resistance of 3-8 M Ω and filled with internal solution containing (in mM): 130 K-gluconate, 10 HEPES, 0 (human) or 0.3 (mouse) ethylene glycol-bis(β -aminoethyl ether)-N,N,N',N'-tetraacetic acid (EGTA), 3 KCl, 0.23 Na₂GTP, 6.35 Na₂Phosphocreatine, 3.4 Mg-ATP, 13.4 Biocytin, and either 50 μ M Cascade Blue dye (excited at 490 nm), or 50 μ M Alexa-488 (excited at 565 nm). Internal solution was measured with osmolarity between 280 and 295 mOsm with pH between 7.2 and 7.3. All electrophysiological values are reported without junction potential correction. We removed EGTA from our internal solution for human recordings to be consistent with previous human electrophysiological studies (9, 10). A small subset of human recordings were conducted with 0.3 mM EGTA. A comparison of connection elements in which we had both EGTA conditions showed consistent connectivity and synaptic properties and thus the data was pooled (Fig S9).

Eight recording headstages were mounted in a semi-circular arrangement around the recording chamber. The pipette holders were fitted with custom shields to reduce crosstalk artifacts. Each headstage was independently controlled using modified triple-axis motors (Scientifica; PatchStar). Recorded signals were amplified (Multiclamp 700B, Molecular Devices) and digitized (50-200 kHz) using ITC 1600 DAQs (Heka). Pipette pressure was controlled using electro-pneumatic control valves (Proportion-Air; PA2193) or, though manual, mouth applied pressure, available for one pipette at a time. Slices were visualized using oblique (Olympus; WI-OBCD) infrared illumination using 40x or 4x objectives on a custom motorized stage (Scientifica) using a digital sCMOS camera (Hamamatsu; Flash 4.0 V2). Acq4 software (acq4.org; (80)) was used for pipette positioning, imaging, and subsequent image analysis.

Eight neurons (excitatory or inhibitory) were targeted based on cortical layer, somatic appearance, and depth from the slice's surface in experiments from human and mouse tissue. Neurons in transgenic mice were also targeted based on fluorescent reporter expression. Cells were targeted with a depth of at least 40 μm (Fig S2B) from the surface of the slice with automated pipette control assistance. In order to minimize tissue distortion and damage, pipettes moved through the tissue on a trajectory that was collinear with the long axis of the pipette with minimal positive pressure (10 - 40 mBar).

Whole-cell patch-clamp electrophysiological recordings were performed on neurons that formed a stable seal and had a successful break-in. At least two neurons were measured at the same time per recording, with the mean number of simultaneous recordings being 4 for both mouse (4.1 ± 1.7 ; SD) and human (4.3 ± 1.8 ; SD) (see Fig 1A for distributions). Recordings were performed with a holding potential set to either -70 mV (to measure excitatory inputs) or -55 mV (to measure inhibitory inputs) and were maintained within 2 mV using automated bias current injection. Data acquisition was collected using Multi-channel Igor Electrophysiology Suite (MIES; <https://github.com/AllenInstitute/MIES>), custom software written in Igor Pro (WaveMetrics). A 15-18 second intersweep interval to allow the synapse to recover was used. During a sweep, evoked action potentials were distributed in time across recordings such that they were separated by at least 150 ms.

To examine short-term plasticity (STP), cells were stimulated in current and voltage-clamp to drive trains of 12 action potentials (Fig 1B) at different fixed frequencies of 10, 20, 50, 100, and 200 Hz with a delay period between the 8th and 9th pulses (81). The delay period lasted 250 ms for all frequencies with additional delay periods (125, 500, 1000, 2000, 4000 ms) for 50 Hz stimulation. Protocols were repeated five times for each stimulation frequency and delay interval. We also delivered a “mixed frequency” stimulus which was composed of 8 action potentials at 30Hz immediately followed by 30 action potentials, whose intervals were a random resequencing of 29 exponentially increasing intervals between 5 and 100 ms. The intervals were fixed across sweeps and experiments. While in current-clamp, an additional set of stimuli was used to characterize intrinsic properties of each cell (Fig 1C). To estimate input resistance of the cell, a 1-second-long hyperpolarizing square pulse was delivered at an initial amplitude of -20 pA while keeping the neuron at -70 mV. The voltage response to each current step was measured online and successive current steps were titrated to target response voltages of -68, -72, -75, -80, and -85 mV so as to reliably activate I_h when present. To measure spiking properties, a long (500 ms) depolarizing square pulse stimulus was delivered that started at rheobase and increased 25 pA for 6 intervals. Lastly, we delivered a 15-second sinusoidal chirp that increased in frequency from 0.2 to 40 Hz and evoked a response magnitude that measured ~ 10 mV from peak to trough. Stimulus protocols were delivered regardless of whether connections were observed during the experiment.

PatchSeq recordings and processing

PatchSeq recordings were performed in a subset of mouse experiments. To avoid sample contamination, surfaces, equipment, and materials were cleaned using DNA away (Thermo Scientific), RNase Zap (Sigma-Aldrich), and nuclease-free water (in that order). aCSF V was made daily and filtered before use. Materials used to make and store aCSF V were cleaned

thoroughly before use. Recording pipettes were filled with ~1.75 μL of RNase Inhibitor containing internal solution: 110 mM K-Gluconate, 4 mM KCl, 10 mM HEPES, 1 mM adenosine 5'-triphosphate magnesium salt, 0.3 mM guanosine 5'-triphosphate sodium salt hydrate, 10 mM sodium phosphocreatine, 0.2 mM ethylene glycol-bis (2-aminoethyl ether)-N,N,N',N'-tetraacetic acid, 20 $\mu\text{g}/\text{mL}$ glycogen, 0.5 U/ μL RNase Inhibitor, 0.5 % biocytin, and either 50 μM Cascade Blue dye (excited at 490 nm), or 50 μM Alexa-488 (excited at 565 nm).

In patchSeq experiments, a subset of stimuli were collected to limit progressive cell swelling associated with the addition of RNase to the internal solution (39).

Methods for nuclei extraction and processing are similar to previous patchSeq studies (39, 63). At the end of the experiment, pipettes were adjusted to the soma center or placed near the nucleus, if visible. A small amount of negative pressure (~0.5 psi) was applied to all pipettes simultaneously for cytosol extraction. Extraction time varied for each cell; pipettes were slowly (~0.3 $\mu\text{m}/\text{s}$) retracted in the x and z-axis once the soma had visibly shrunk and/or the nucleus was visible at the tip of the pipette. Once pipettes were out of the slice, cytosol and/or nucleus content in each pipette were expelled into individual PCR tubes containing 11.5 μl of lysis buffer (Takara, 634984) and stored in -80 $^{\circ}\text{C}$.

We used the SMART-Seq v4 Ultra Low Input RNA Kit for Sequencing (Takara, 634894) per the manufacturer's instructions to reverse transcribe RNA and amplify full-length cDNA. To obtain detailed methods, see <http://celltypes.brain-map.org>, "Transcriptomics Overview Technical White Paper". We identified transcriptomic types by mapping our Patch-seq transcriptomes data in the same methods mentioned in previous studies (63, 82).

Histology and imaging

After electrophysiological recordings, slices were fixed in solution containing 4% paraformaldehyde and 2.5% glutaraldehyde for at least 40 hours at 4 $^{\circ}\text{C}$. Slices were then transferred and washed in phosphate buffer saline (PBS) solution for 1-7 days before staining.

A 3,3'-diaminobenzidine (DAB) peroxidase substrate kit (Vector Laboratories) generated a brown reaction product in biocytin-filled neurons. Slices were stained with 5 μM 4',6-diamidino-2-phenylindole (DAPI) in PBS for 15 min at room temperature and then triple-washed in PBS (10 min for each wash). Slices were then transferred to 1% hydrogen peroxide (H_2O_2) in PBS for 30 min and triple washed in PBS. Afterward, slices were mounted onto gelatin-coated slides and cover-slipped with Aqua-Poly/Mount (Polysciences). Slides were dried for approximately 2 days before imaging.

Mounted slides were imaged on an Axiomager Z2 microscope (Zeiss) equipped with an Axiocam 506 monochrome camera. Tiled mosaic images of whole slices were captured with a 20x objective lens (Zeiss Plan-NEOFLUOR 20x/0.5) to generate both biocytin-labeled images and DAPI-labeled images. Biocytin images were used to assess cell morphology and DAPI images were used to identify cortical layer boundaries. To further classify cell morphology, we also used a 63x lens to capture high-resolution z-stacks of biocytin filled cells, which were stitched together using ZEN software and exported as single-plane TIFF files.

Connection detection

Electrophysiology data was filtered through multiple quality control (QC) steps to ensure it was of good quality to detect a connection (Table S4). Additional QC criteria were applied for characterizing connections which are discussed in the following section.

Initial data processing consisted of manual connection detection and curve fitting (Fig 1B *Pair Processing*) using our [Pair Analysis Tool](#) (Fig S10). During recording, cells were held at -70 mV to probe excitatory connections or -55 mV to probe inhibitory connections. Within each clamp mode (voltage and current) data was binned into two ranges of recorded membrane potentials [-80, -61] (-70 mV holding potential) and [-60, -50] (-55 mV holding potential). Within each of these four groups, individual postsynaptic responses (PSC/P, Fig S10 white traces) from stimuli ≤ 50 Hz were aligned to the peak rate of rise of the presynaptic spike and averaged (Fig S10A blue traces). Only QC passed PSC/Ps were included in the average. Users visually identified chemical and electrical connections from the average postsynaptic responses in each of the four quadrants and marked whether the connection was excitatory or inhibitory. Manual connectivity calls were used to train a machine classifier (13), which could reveal possible false positives or negatives that were later manually re-evaluated.

Connection characterization

Users manually identified the onset of detected connections' postsynaptic response (Fig 1B, Fig S10, yellow line). This user-defined latency was used to initialize an automated curve fit of the average response constrained to $\pm 100 \mu\text{s}$ of the user-defined latency (Fig S10B red and green traces). The user inspected the automated fit for a good match to the average and could refit as necessary. Once the user was satisfied with the output, the fit was manually passed (Fig S10B green) or failed (Fig S10B red). Contamination by electrical connections or artifacts, the shape of the fit, and other factors were considered when deciding whether to pass or fail the fit. Users were also able to make notes, which were used to update and test new fitting algorithms.

Passing postsynaptic response fits were used to characterize strength, kinetics, and short-term plasticity of the connection in a multi-stage process aimed to maximize data inclusion for each characteristic. Kinetics, rise time and decay tau, were measured as a weighted average of curve fit parameters from the two membrane potential ranges. Latency was similarly measured as a weighted average across not only membrane potentials but clamp mode as well, as we did not expect PSC/P onset to be influenced by these conditions. Latency values from the individual membrane potential/clamp mode modalities were confirmed to be within 200 μs of each other to be included in the weighted average. Thus, each connection has a singular latency value.

Connection strength was measured as the PSC/P amplitude at a “resting state” to avoid the influence of short-term plasticity in our estimate of strength. Individual PSC/Ps recorded at the appropriate holding potential range for the connection type (-60 to -50 mV for inhibitory, -80 to -50 mV for excitatory) and preceded by at least 8 seconds of quiescence were aligned to the presynaptic spike and averaged. This reduced average was fit with kinetic parameters initialized to those from the fit to the average of all responses. For connection types that show short-term

facilitation, the resting state amplitude is often very small and thus, we calculated a second metric to capture the near maximum strength that a connection can produce. For this, individual PSPs were fit with parameters initialized by results of the average fit. We then calculated the 90th percentile of fit amplitudes to approximate maximum strength (this value was also used to normalize our estimate of short-term plasticity discussed below). The measured amplitude for inhibitory connections is further affected by the driving force. We thus calculated two additional metrics that are independent of the driving force using the measured reversal potential for each connection. Reversal potential was calculated from series-resistance-adjusted voltage-clamp data in which we had responses measured over a broad range of holding potentials (-80 to -50 mV) (Fig S11A). The reversal potential was then used to calculate the effective conductance for each connection in current clamp as the slope of the line between [avg baseline potential, resting PSP amplitude] and [reversal potential, 0]. This effective conductance measurement could further be used to calculate an adjusted resting state PSP amplitude at the targeted holding potential of -55 mV for inhibitory connections (Fig S11B). Both the effective conductance and adjusted PSP amplitude show good correlation with resting state PSP amplitude mentioned above (Fig S11C). The slope of the regression line between resting state PSP amplitude and adjusted PSP amplitude is 0.94, giving us confidence that the effect of driving force on inhibitory strength is minimal. Similarly, a matrix of inhibitory adjusted PSP amplitude shows similar patterns to our matrix of resting state PSP amplitude (Fig S11D, Fig 3D) suggesting that differences in inhibitory strength as a function of cell subclass are not largely influenced by systematic differences in driving force.

Short-term plasticity (STP) was measured from current-clamp PSPs in response to trains of stimuli at multiple frequencies consisting of eight pulses, followed by a variable delay, and then four more pulses (Fig 1B *Multipatch Experiment, Connection Analysis*). Quantifying the magnitude of STP has taken several forms from a paired-pulse ratio (PPR, ratio of the second response to the first), to a ratio of the last pulse in a train to the first. These ratios are sensitive to noise, especially when the signal in the denominator becomes very small; thus we quantified STP using the difference between late (pulses 6-8) and initial response amplitudes, normalized by the 90th percentile response amplitude (Fig 1B), termed STP induction. STP induction was measured from the amplitude of individual PSP fits as follows (Fig 1B *Connection Analysis*):

$$\frac{\text{Avg}(6\text{th}, 7\text{th}, 8\text{th pulse amplitudes}) - 1\text{st pulse amplitude}}{90\text{th percentile amplitude}} \quad (1)$$

By this calculation positive values denote facilitating connections and negative values depressing.

Recovery from STP was similarly calculated from individual PSP fits as:

$$\frac{\text{Avg}(9\text{th} - 12\text{th pulse amplitudes}) - \text{Avg}(1\text{st} - 4\text{th pulse amplitudes})}{90\text{th percentile amplitude}} \quad (2)$$

This yields positive values indicative of recovery beyond the initial state of the connection and negative values where the connection has not yet recovered from STP.

PSP/C variability is typically reported as the coefficient of variation (CV) of response amplitudes; however, for weak connections the CV is dominated by noise arising from multiple factors including the release probability, quantal variance, and other biological and electrical

sources (84). To access the component of the variability driven by synaptic release mechanisms, we calculated an “adjusted coefficient of variation” (aCV) that subtracts the experimental noise contribution before normalization:

$$aCV(amps, noise) = \frac{\sqrt{\sigma_{amps}^2 - \sigma_{noise}^2}}{\mu_{amps}} \quad (3)$$

Where μ_{amps} and σ_{amps} are the mean and standard deviation of response amplitudes, and σ_{noise} is the standard deviation of background noise, which is measured by performing the same amplitude measurement algorithm on regions of the recording that have no presynaptic stimulus (47).

For the purposes of analyses in Figures 3 and 4, transgenic cell subclass was used to identify the pre- and postsynaptic cell type resulting in semi-layer-specificity of E-I and I-E connections while pooling I-I connections across all layers. Pooling was motivated by the observed homogeneity of intralaminar I-I connections across layers (Fig S12, S13) and allowed for more robust comparisons. Nevertheless, pooled results may contain layer-related biases due to differences in the laminar distribution of cell bodies across the inhibitory subclasses. For example, most Vip cells are located in L2/3 (Fig S12A) and thus connections involving these cells may be biased toward upper layers (65, 66).

The strength of electrical connections (gap junctions) was quantified as a coupling coefficient and junctional conductance (40, 62). The voltage change from baseline evoked by a subthreshold long-pulse current injection (Fig 1C) was measured in both the pre- and postsynaptic cell. The coupling coefficient was measured as a least squares linear regression of the voltage change across all sweeps. For cells in which we also measured input resistance the junctional conductance was calculated as $G_j = (1/R_2) \times CC / (1 - CC)$ (83) where CC is the coupling coefficient and R2 is the input resistance of the postsynaptic cell.

Cell characterization

Transgenic Expression and Cell Subclasses

Stack images of the recording site were taken in brightfield, epifluorescence (tdTomato and EGFP), and dye-filled recording pipettes. These images were filtered and overlaid on top of each other (Fig 1B *Multipatch Experiment*) to display the recording site and targeted cells. From the overlap of epifluorescence and pipette dye, we identified each cell's transgenic expression, which was used to define its subclass. If fluorescence overlap could not be confirmed, the expression was marked as unknown.

All mouse L2/3 excitatory cells and human cells were fluorescence-negative cells and thus, morphological features were used to identify these cells as discussed below. Human cells without morphological characterization were categorized as excitatory or inhibitory based on observed PSPs to expand the dataset for analysis of synaptic properties, but not for analysis of connectivity where this would bias results. Human cells without morphological characterization were categorized as excitatory or inhibitory based on observed PSPs to expand the dataset for analysis of synaptic properties, but not for analysis of connectivity where this would bias results. Human

excitatory cells were split into putative subclasses by layer. The inhibitory cells in human, expected to be primarily fast-spiking Pvalb cells due to their prevalence, were pooled across layers based on the consistency of inhibitory synaptic properties through the cortical depth observed in the mouse data (Fig S12, S13). Due to experimental constraints from tissue health and imaging challenges, sampling was primarily from the supragranular layers of cortex, and some deep subclasses were under-represented. The L6 subclass was dropped from all analyses, and the L4 subclass from synapse property analyses.

Electrophysiology

Intrinsic characterization of individual cells was carried out similarly to that described in (84). Although we did not collect the full suite of stimuli, the long-pulse sweeps we acquired were sufficient to calculate subthreshold properties such as input resistance, sag, and rheobase; spike train properties such as f-I slope and adaptation index; and single spike properties such as upstroke-downstroke ratio, after-hyperpolarization, and width (Fig1C *Intrinsic Ephys*). For spike upstroke, downstroke, width, threshold, and ISI, ‘adaptation ratio’ features were calculated as a ratio of the spike features between the first and fifth spike. A subset of cells also had subthreshold frequency response characterized by a logarithmic chirp stimulus (sine wave with exponentially increasing frequency), for which the impedance profile was calculated and characterized by features including the peak frequency and peak ratio. Feature extraction was implemented using the IPFX python package (<https://github.com/AllenInstitute/ipfx>); custom code used for chirps and some high-level features will be released in a future version of IPFX.

For the human cell dataset, all electrophysiology features were aggregated and visualized using a UMAP projection to gain perspective on the electrophysiological cell type (‘e-type’) distinctions present. Cells with more than 25% missing features were dropped. The remaining missing features were imputed as a distance-weighted mean of 3 nearest neighbors, and each feature was independently power transformed to a standard Gaussian. Features uninformative for known cell-type distinctions were dropped (assessed by F-score of ANOVA against layer and spinness labels), and the remaining features were visualized by UMAP projection. For the L2/3 focused analysis, the L2/3 pyramidal subclass was refined by an upper bound on input resistance of 225 M Ω , excluding L4-type cells that can overlap into L3 based on their smaller size and higher input resistance (50). These refined subclasses were visualized in the full UMAP feature space and used for the depth correlation analysis.

Morphology and Position

Cell morphology was qualitatively assessed from 63x maximum projection image z-stacks of biocytin filled cells and included features such as dendritic type (spiny-ness), axon origination point of inhibitory cells, and length of truncated axon (measured in pixels as a straight line from axon origination point to truncation and multiplied by image resolution to obtain distance in μm) (Fig 1C *Morphology*). Aspiny or sparsely spiny cells (inhibitory) were defined as such if their dendrites lacked or only had few protrusions. Spiny (excitatory) cells have frequent dendritic protrusions as well as an apical dendrite (85, 86). For the purposes of cell classification throughout our results, "spiny-ness" refers to this analysis. Layer 2/3 pyramidal cells in mouse were largely identified as being “spiny” as we did not have a transgenic driver for this layer.

Similarly in human, all pyramidal cells are identified by their dendritic spiny-ness and by the presence/absence of an apical dendrite. A full list of morphological classification can be found in Table S5.

Cortical layer boundaries were determined from DAPI images, with the top of Layer 1 serving as a marker of pia and the bottom of Layer 6 as a marker of white matter. During the experiment, cell position was recorded in the fluorescent images' reference space (Fig 1B *Multipatch Experiment*) and later coregistered with the DAPI image. Image coregistration enabled the cell soma layer to be established. Other positional metrics such as intersomatic distances (vertical and lateral), distance from pia and white matter, fractional cortical depth, and depth within the layer were also calculated from the soma position and layer boundary data using the `neuron_morphology` python package (https://github.com/AllenInstitute/neuron_morphology). Depth measurements were made using streamlines from the pia to WM boundaries (or the nearest layer boundary in cases where not all layers were complete in the slice). For each cell pair, the pia-WM orientation from the streamlines was averaged and used as a 'vertical' orientation to decompose the soma-soma separation into vertical and lateral distances.

Connection probability estimation

We estimated the connection probability through modeling a probability distribution that depends on the experimental conditions such as the intersomatic distance, depth of the neurons in slices, background electrical noise, and the number of postsynaptic responses that could be averaged together. To build a model for the connection probability, we started with a log-likelihood function of the binomial distribution, constructed its probability using multiple experimental variables, and estimated model parameters using maximum-likelihood estimation (MLE).

The log-likelihood function for the binomial distribution is defined as follows.

$$l(\theta|x) = \sum_{i=1}^{n_{conn}} \log(p(\theta|x_{conn_i})) + \sum_{j=1}^{n_{unc}} \log(1-p(\theta|x_{unc_j})) \quad (4)$$

where θ is a set of model parameters, x is a set of experimental variables associated with each pair, p is the model estimate of the connection probability, n_{conn} and n_{unc} are the numbers of connected and unconnected pairs, x_{conn} and x_{unc} are subset of x for connected and unconnected pairs, respectively. The first sum runs over connected pairs; the second sum runs over unconnected pairs. Below, we elaborate how this probability function is constructed.

Gaussian model with maximum likelihood estimation

Connection probability as a function of lateral intersomatic distance of a pair was modeled as a Gaussian function centered at 0 distance:

$$p(\theta|x) = p_{max} e^{\frac{-d^2}{2\sigma^2}} \quad (5)$$

where $\theta = \{p_{max}, \sigma\}$ and $x = \{d\}$, p_{max} is the peak connection probability, σ is the distance constant of connection probability, and d is the lateral intersomatic distance of the pair.

The number of samples (pairs of cells) included in the model has a profound impact on our confidence in the model outputs, p_{max} and σ . We used simulated distances drawn from the distribution of measured intersomatic distances and a defined p_{max} and σ to assess the possible error in our fits. We found that while p_{max} was fairly well constrained, σ was not, particularly for lower numbers of samples. We therefore chose to use a fixed σ value for groupings at the subclass level (Fig 2B), which further constrained the fit of peak connection probability. To determine the fixed σ value, we pooled our data from mouse into four categories based on the cell class of the presynaptic and postsynaptic cells, namely excitatory to excitatory (5,619 cell pairs), excitatory to inhibitory (2,238 pairs), inhibitory to excitatory (2,035 pairs), and inhibitory to inhibitory (6,791 pairs). This allowed us to have several thousand samples in each group to obtain a better estimate of σ (Fig 2A). This showed a trend for shorter σ values for within EI-class connections and longer σ values for across EI-class. In order to more fully determine if the σ of these four groups could have been drawn from the same distribution we simulated 10,000 experiments with a true σ that varied between those measured from experimental data. We then did a pair-wise comparison of the σ ratio for each unique comparison among the four groups and calculated the percentile of this distribution where the measured ratio fell. When correcting for multiple comparisons we found that while the I→I and I→E connectivity profiles likely have σ that are not drawn from the same distribution, we could not rule that out for the other comparisons. This analysis was also conducted for a comparison of chemical versus electrical connections among inhibitory cells, with 1,000 simulated trials. From this analysis we chose to fix σ for individual matrix elements of chemical connections (Fig 2B) to 97 μm for within class and 125 μm for across class, and to fix σ for electrical connections (Fig S4A) to 75 μm . A similar procedure was conducted for human data, resulting in a fixed σ of 130 μm (Fig 5A).

A unified model of connection probability adjustment

We extended the analysis of the connection probability as a function of intersomatic distance to include the effect of tissue slicing and false negative detection of connections due to background noise. We created a unified model that applies these adjustments to the connection probability, as a function of the pair distance (discussed above), the presynaptic axon length, the depth of the cells from the slice surface, and the detection power. Using the same log-likelihood function described above, we extended the probability to the following.

$$p(\theta|x) = p_{max} e^{\frac{-d^2}{2\sigma^2}} \prod_k C_k(\theta_k|x_k) \quad (6)$$

where $\theta = \{p_{max}, \sigma, \rho_{ax}, \mu_{depth}, \sigma_{depth}, \mu_{det}, \sigma_{det}\}$, $x = \{d, l_{ax}, z_{depth}, p_{det}\}$, and product over k runs over the following three corrections factors. The correction functions C_k , their parameters k , and their variables x_k are described below.

The model for the presynaptic axon length is a binary step function with a threshold at 200 μm as axons were not measured past this point (Table S5). Also, because the number of neurons with axons measured less than 200 μm were few, we did not have sufficient data to determine the function shape below this threshold. Therefore, we used a single adjustment ratio for the correction.

$$C_{ax}(\rho_{ax}|l_{ax}) = 1(l_{ax} > 200 \mu m), \text{ or } \rho_{ax}(l_{ax} > 200 \mu m) \quad (7)$$

The model for the average depth of the pair of neurons is as follows.

$$C_{depth}(\mu_{depth}, \sigma_{depth}|z_{depth}) = \frac{1}{2} \left(1 + \operatorname{erf} \left(\frac{z_{depth} - \mu_{depth}}{\sqrt{2} \sigma_{depth}} \right) \right) \quad (8)$$

where erf is an error function:

$$\operatorname{erf}(x) = \frac{2}{\sqrt{\pi}} \int_0^x e^{-t^2} dt \quad (9)$$

The detection power (that is analogous to signal-to-noise ratio) is defined as

$$p_{det} = \frac{\sqrt{N_{pre}}}{\sigma_{post}} \quad (10)$$

where N_{pre} is the number of presynaptic test spikes and σ_{post} is the background noise-level of the postsynaptic neuron, measured as the standard deviation of recording data from quiescent periods with no stimulation. The number of presynaptic test spikes influences detectability of connections through averaging. As more spikes are delivered over the course of an experiment, more postsynaptic responses are available to be averaged to see the resulting, and often small, synaptic response above the level of background noise which will be averaged out (Fig S14A). In this way, our ability to detect a synapse is inversely proportional to the background noise amplitude, and directly proportional to the square root of the number of averaged responses (Fig S14C).

Background noise has several sources, some biological, and others technical and varied over an order of magnitude from cell to cell (Fig S14B). Nonetheless, this variance is quite stable overall when comparing across rigs, manipulators, and operators (Fig S14D), suggesting a relatively small noise contribution from technical sources. In contrast, background noise varies substantially when comparing across cell subclasses. For example, Vip (0.89 [0.67, 1.23] mV; median [IQR]) and Sst (0.8 [0.59, 1.07] mV) tend to have high noise, whereas Pvalb (0.48, [0.38, 0.60] mV) and L2/3 excitatory cells (0.45 [0.32, 0.65] mV) tend to have low noise.

The model for the detection power p_{det} is also an error function, but in a log space, because the synaptic weight distribution is expected to be a log-normal distribution.

$$C_{det}(\mu_{det}, \sigma_{det}|p_{det}) = \frac{1}{2} \left(1 + \operatorname{erf} \left(\frac{\log_{10}(p_{det}) - \mu_{det}}{\sqrt{2} \sigma_{det}} \right) \right). \quad (11)$$

We did not see a saturation of the connection probability when the presynaptic cell was inhibitory (Fig S2D), suggesting that there are potentially a large number of undetected synapses. However, we did not want to overestimate the connection probability in the range of detection power where we did not have sufficient data. Therefore, we applied the following constraint to the fit.

$$\mu_{det} + \alpha \sigma_{det} < \beta \quad (12)$$

Where $\alpha \sim 0.6745$, specifying the quartile of the integrand Gaussian of the error function, and $\beta \sim 4.6613$, specifying the quartile of the detection power distribution in our data. This constraint ensures saturation in the high detection power region where data are scarce.

The models and the parameters for these three corrections are determined individually for each variable (Fig S2B-D) and incorporated into the likelihood function used for the distance adjustment (Fig S2A). When we estimated final p_{max} , we performed a single-parameter MLE, fixing all the other model parameters to pre-determined values. Four models were used for mouse connectivity reflecting the varying effects that each variable has on excitatory versus inhibitory and within versus across class. Matrix elements at the subclass level (Fig 2B, S2A) were determined to be one of E→E, E→I, I→E, or I→I and the appropriate model was applied to adjust p_{max} (Fig S2F).

In the case of human connections, the data was insufficient to fully constrain the complete connection probability adjustment model, and we applied an adjustment for lateral intersomatic distance only. However, calculations suggested that the remaining adjustments are likely much smaller than in the mouse dataset (<50%) due to higher detection power arising from lower noise and more recorded spikes.

Estimating connection probability and confidence intervals

The goal of optimizing the Gaussian MLE was to compare connection probabilities across different cell groups that may have been sampled at different intersomatic distances and have variable presynaptic axon lengths and detection power. Thus, in addition to fitting p_{max} we wanted to calculate a confidence interval of connection probability. Our initial approach was to analyze hundreds of resampled iterations of data from each matrix element. However, this method is computationally expensive and starts to break down when connection probability or the number of samples is very low. We determined the confidence intervals based on the log-likelihood function (87), assuming our log-likelihood function is asymptotically proportional to the χ^2 -distribution ($-2l(p_{max}|x) \sim \chi^2(p_{max})$; Wilks' theorem (88)). Namely, we estimated upper and lower bounds of the CI as $p_{max,CI}$ such that

$$2l(p_{max,CI}|x) = 2l(p_{max}|x) - 3.84 \quad (13)$$

Where 3.84 is 95-percentile of the χ^2 -distribution with one degree of freedom. The computation of the CIs are done by MINOS algorithm in iminuit package (<https://github.com/scikit-hep/iminuit>). The estimated confidence intervals were used to shade connection probability heatmaps in Figure 2B, 5A, and Figure S1A.

The parameter optimization can result in values for p_{max} (or CI bounds) greater than 1 in cases where the data is not well fit by the fixed-width Gaussian, typically because a class of connections has either low sampling or a true underlying connection probability function with a distinct shape or size. In the resulting figures (Fig 2B, 5A, S1A), p_{max} values and CI upper bounds were clipped at 1, reflecting the fact that such data should be better fit by a flat-topped curve that approaches 1 at its maximum (Fig S1B). The unclipped values are available in our data and code release for applications like modeling, where estimating the true connection probability vs. distance function may be more important than interpretation of p_{max} as a probability.

Modeling synapse behavior

Stochastic quantal release model

We developed a model of stochastic vesicle release and synaptic dynamics that expands upon standard models (89) and is similar to some recent models (52, 53, 56). The model was designed to meet several criteria. First, it should give estimates of synaptic quantal parameters (number of release sites, probability of release, and quantal size) and dynamic parameters (facilitation, docking, etc.). The quantal parameters alone allow the model to predict the overall distribution of response amplitudes (Fig S7A). By allowing quantal parameters to change in response to the history of activity, the model is able to account for changes in the response distribution (Fig S7B,C). Next, the model should operate on individual spike times and response amplitudes rather than requiring structured or repeated stimuli. This ensures that the model can access the complete distribution of response amplitudes and any correlations between adjacent responses.

Additionally, operating on individual events rather than averages ensures that we use all available data for each connection, regardless of the applied stimuli. Finally, the model should fail gracefully in cases with low signal-to-noise ratio by indicating low confidence over its parameters rather than returning unreliable values.

We begin with a standard quantal model with three parameters: N , the number of release sites; q , the amplitude of the postsynaptic response to a single vesicle, and P_r , the probability that each release site will release a vesicle in response to one action potential. We make simplifying assumptions that all release sites in a connection share the same values of P_r and q , and that the response to multiple vesicles released simultaneously is simply the linear sum of individual responses. This component of the model simply predicts that the number of vesicles released per spike is defined by a binomial distribution with parameters N and P_r , and that the distribution of response amplitudes is the same with an additional scaling factor q .

The measured response amplitudes in our dataset only occasionally show binomial characteristics; however in most cases, background recording noise and quantal variability obscure the underlying discrete distribution. We model these sources of variability as independent Gaussian distributions for measurement noise and quantal variance, with parameters σ_m and σ_q , respectively. These combine with the binomial distribution to make a weighted Gaussian mixture model that, on its own, does a decent job of approximating the overall distributions of event amplitudes. The model response amplitude probability distribution $P(X; \theta)$ is calculated as:

$$\text{normpdf}(\mu, \sigma, x) = \sqrt{\frac{1}{2\pi\sigma^2}} e^{-\frac{(x-\mu)^2}{2\sigma^2}} \quad (14)$$

$$\text{binompmf}(n, p, k) = \frac{n!}{k!(n-k)!} p^k (1-p)^{n-k} \quad (15)$$

$$P(X; \theta) = \sum_{k=0}^N \text{binompmf}(N, P_r, k) \text{normpdf}(kq, \sqrt{k\sigma_q^2 + \sigma_m^2}, X) \quad (16)$$

Short term plasticity

Synapses undergo short term plasticity, which we model as changes in the expected distribution of response amplitudes over time (89). Each incoming action potential causes an instantaneous modification to the quantal parameters N and P_r , which then recover back to their initial values by exponential decay until the time of the next action potential. Although we only seek a phenomenological description of the synapse, this description is designed to mimic three major classes of synaptic dynamics: vesicle depletion, facilitation, and calcium channel inactivation. Vesicle depletion is implemented by using the response amplitudes and q to estimate the most likely number of released vesicles following each spike, which is then subtracted from the releasable vesicle pool. Recovery from vesicle depletion is modeled as an exponential with time constant τ_r . Facilitation and calcium channel inactivation increase or decrease the release probability, respectively, for every incoming spike, and decay back to the initial release probability with time constants τ_f and τ_i . In addition to the decay time constants, these mechanisms introduce an extra two parameters: the amount of facilitation a_f and inactivation a_i per spike. The complete algorithm then looks like:

- a. Initialize state variables:
 - i. $N_j = N_r$
 - ii. $depression = 0$
 - iii. $facilitation = 0$
- b. For each spike j at time t_j :
 - i. Let $dt = t_j - t_{j-1}$
 - ii. Recover state variables:
 1. $N_j += (N_r - N_j) * (1 - e^{-dt/\tau_D})$
 2. $depression *= e^{-dt/\tau_D}$
 3. $facilitation *= e^{-dt/\tau_F}$
 - iii. Let $P_j = (1 - depression) * (P_r + (1 - P_r) * facilitation)$
 - iv. Define distribution parameters $\theta = \{N_j, P_j, q, \sigma_q, \sigma_m\}$
 - v. Estimate likelihood of measured response amplitude $P(Amp_j | \theta)$ or generate a random sample drawn from $P(\theta)$
 - vi. Apply post-spike modifications to state variables:
 1. $vesicle_pool -= Amp_j / q$
 2. $depression += a_D * (1 - depression)$
 3. $facilitation += a_F * (1 - facilitation)$

Occasionally a presynaptic stimulus is not followed by a detectable spike, which could be caused by a genuine spike failure or simply by a failure of the spike detection algorithm. In these cases, we assume that a spike did occur for the purpose of updating the model state variables, but we incur a short timeout during which we stop accumulating evidence toward the overall model likelihood.

For any combination of parameters, we estimate a *likelihood* that a recorded set of amplitudes $A_{1..m}$ could be generated by the model by the mean log probability density for each response:

$$L(A) = \frac{1}{m} \sum_{j=1}^m \ln(P(A_j)) \quad (17)$$

If most response amplitudes fall within the modeled regions of high probability density, then the total likelihood for that parameter set will be high. Low-likelihood models result from either bad parameters (where response amplitudes fall in low density regions of the model probability distribution) or from insufficiently selective parameters (where the probability distribution is spread out over too much area).

Parameter search and optimization

With a measure of model likelihood, we can now attempt to find a set of parameters that maximize this value, yielding a model that best explains the data. Most prior methods use a metric similar to the likelihood defined above along with an optimization method to efficiently find a single point in the parameter space that is most consistent with the recorded data. However, minimization is notoriously difficult in this domain because the model parameters are underconstrained--there exist many solutions that adequately explain the recorded data, and thus large differences in the optimal parameters may simply result from noise or experimental artifacts, rather than physiological differences between connections (56, 90). To avoid this outcome, we measure the model performance at every point in a large parameter space, thereby identifying the region of the parameter space consistent with the responses recorded from each connection (Fig. S7D). This is similar to some recent methods (52, 53), but differs in that we have implemented a simpler (and thus less computationally expensive) model in order to test many more parameter combinations uniformly.

All combinations of the parameters in a 7-dimensional space were tested, for a total of 6.2 M model tests per connection. At every point in this parameter space, the quantal amplitude q was estimated and optimized using a minimization algorithm (scikit.optimize). Although this minimization strategy fails to find reliable optima when operating over several parameters, we found it to be reliable in the context of this simpler single-variable optimization. The resulting records for each connection thus include measured model likelihood as well as the optimal value of q at each point in the parameter space. This yields an 8 dimensional image that serves as a "fingerprint" describing the unique dynamics of each connection. The size of the parameter space and the number of connections in our dataset together make this a computationally expensive operation. To reduce this cost, we optimized the core routines used in the model using the python packages numpy and numba.

Synapse typing

To visualize the relationship between cell subclass and connection properties, we used the UMAP dimensionality reduction method to organize our connections into a 2 dimensional space for visualization. For each connection, the vesicle release model described above was run on a large parameter space, yielding 6.2 million "features" that collectively describe the regions of parameter space that are (and the regions that are not) compatible with the recorded data. We then used sparse PCA to reduce this down to 50 features. This set of features provides a fingerprint of any information available to the release model, including synaptic strength, stochasticity, and short-term plasticity. Finally, all features were normalized (scikit-learn), then passed to UMAP for the final dimensionality reduction. The resulting 2D space could then be visualized alongside other synaptic and cellular features to investigate the structure inherent in the data. To verify this structure is not an artifact of the reduction to two dimensions, we repeated the analysis for three dimensions but found a similar 2D structure flattened in 3D space.

To verify relationships between connection properties and pre/postsynaptic cell subclasses, we trained a series of classifiers to distinguish specific sets of subclasses. Connection properties were generated from the stochastic release model using the maximum likelihood parameters found for each connection(see Modeling Synapse Behavior above). Properties Included the maximum likelihood parameters, metrics of STP and variability generated from simulated PSP amplitudes (the same metrics used to characterize STP and variability in recorded data), and additional metrics derived from quantal release parameters ($strength=NP_rq$; $quanta_per_spike=NP_r$; $sites_pr_ratio=N/P_r$). A subset of these properties (described below) were normalized and used to perform logistic regression (scikit-learn) to distinguish between different groups of subclasses using a stratified 5-fold cross validation. The regression was then repeated on the same data with shuffled classes, and the original accuracy was compared to the shuffled accuracy to give a percent gain in accuracy over random chance:

$$accuracy_{gain} = 100 \frac{mean(accuracy) - mean(shuffled\ accuracy)}{1 - mean(shuffled\ accuracy)} \quad (18)$$

In this way, we characterized the overall strength of the relationship between synaptic properties and pre/postsynaptic subclasses.

To evaluate the contribution of individual properties to this relationship, the same logistic regression was performed with a single feature at a time and the shuffled accuracy was repeated many times to estimate a null distribution. This analysis provided both a measure of accuracy gain for individual features as well as the probability that each feature accuracy value could have been obtained if it had no relationship to the output class.

Fig. S1

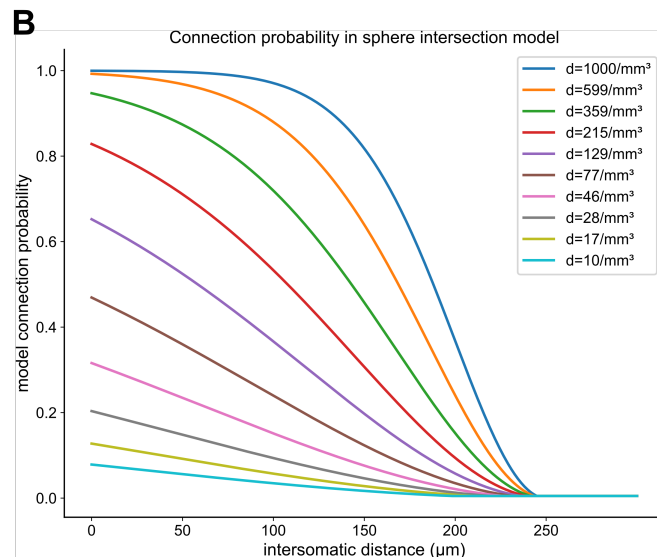
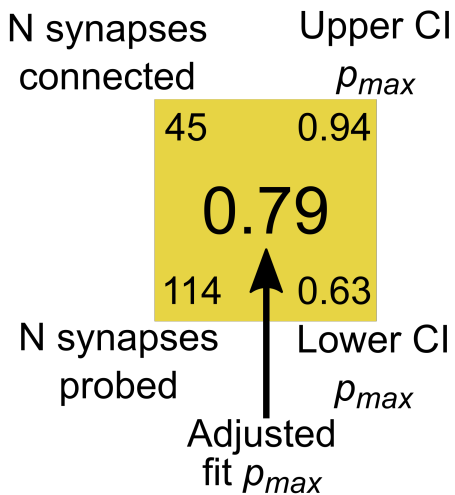
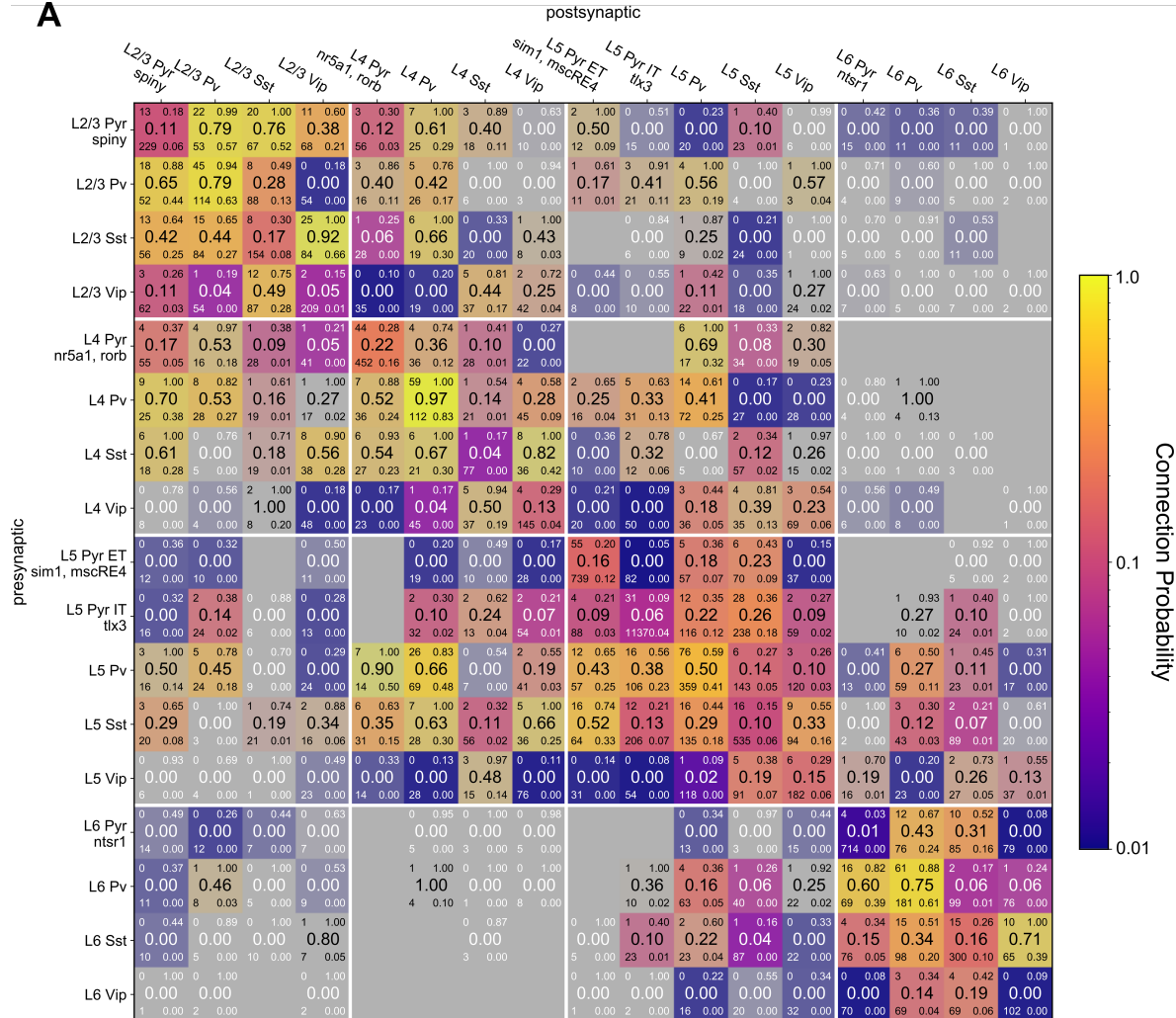


Fig. S1. Connectivity Matrix. A. The connectivity matrix in Fig 2B with additional details highlighted in the expanded element below the matrix. The center number is the fully adjusted (see Figure S2) p_{max} . The upper and lower numbers on the left of each element are the number of connections found (upper) and number of connections probed (lower). The numbers on the right of each element are the upper and lower 95% confidence interval, respectively. B. Connection probability versus intersomatic distance in a simplified model that assumes a constant density of connections inside the volume intersection of two spheres. Changing the density of connections can result in profiles that look qualitatively like an exponential decay, a Gaussian, or a sigmoid.

Fig. S2. Connectivity Adjustments. **A.** From left: Distribution of lateral intersomatic distance (vertical dotted line denotes median throughout row). Connection probability as a function of intersomatic distance for E→E, E→I, I→E, and I→I pairs and 95% confidence interval (grey line/shading) with thresholded fit in the colored line. Fit for the relationship between connection probability and intersomatic distance was a Gaussian. Horizontal dotted line denotes fit p_{max} . Raster below plot shows intersomatic distance of pairs that were probed for connectivity along with pairs that were connected. **B.** Same plots as A for presynaptic axon length measured from biocytin fills. If the axon was measured to at least 200 μm the axon was not measured further except in rare occasions. Fit for the relationship between connection probability and presynaptic axon length was a step function at 200 μm . **C.** Same plots as A for the average depth of the cell pair from the slice surface. In this case the relationship between connection probability and average pair depth is fit with an error function. **D.** Same plots as A for detection power. Detection power combines the background noise of the postsynaptic cell with the number of spikes elicited by the presynaptic cell to probe the connection (see Methods). Detection power as a function of connection probability was also fit with an error function. **E.** Comparison of model fit p_{max} (solid bar) to p_{max} of data filtered above the median (open bar; vertical dashed lines in A-D; in the case of intersomatic distance inclusion was for distances shorter than the median) for each feature in A-D compared to raw connection probability (connected / probed). This highlights the overall effect that each feature has on peak connection probability. The pink bars show p_{max} for the full model (see Methods). Error bars denote 95% confidence interval. **F.** Adjustment factor of each feature applied to each element in the matrix in Fig 2B and Fig S1A.

Fig. S3

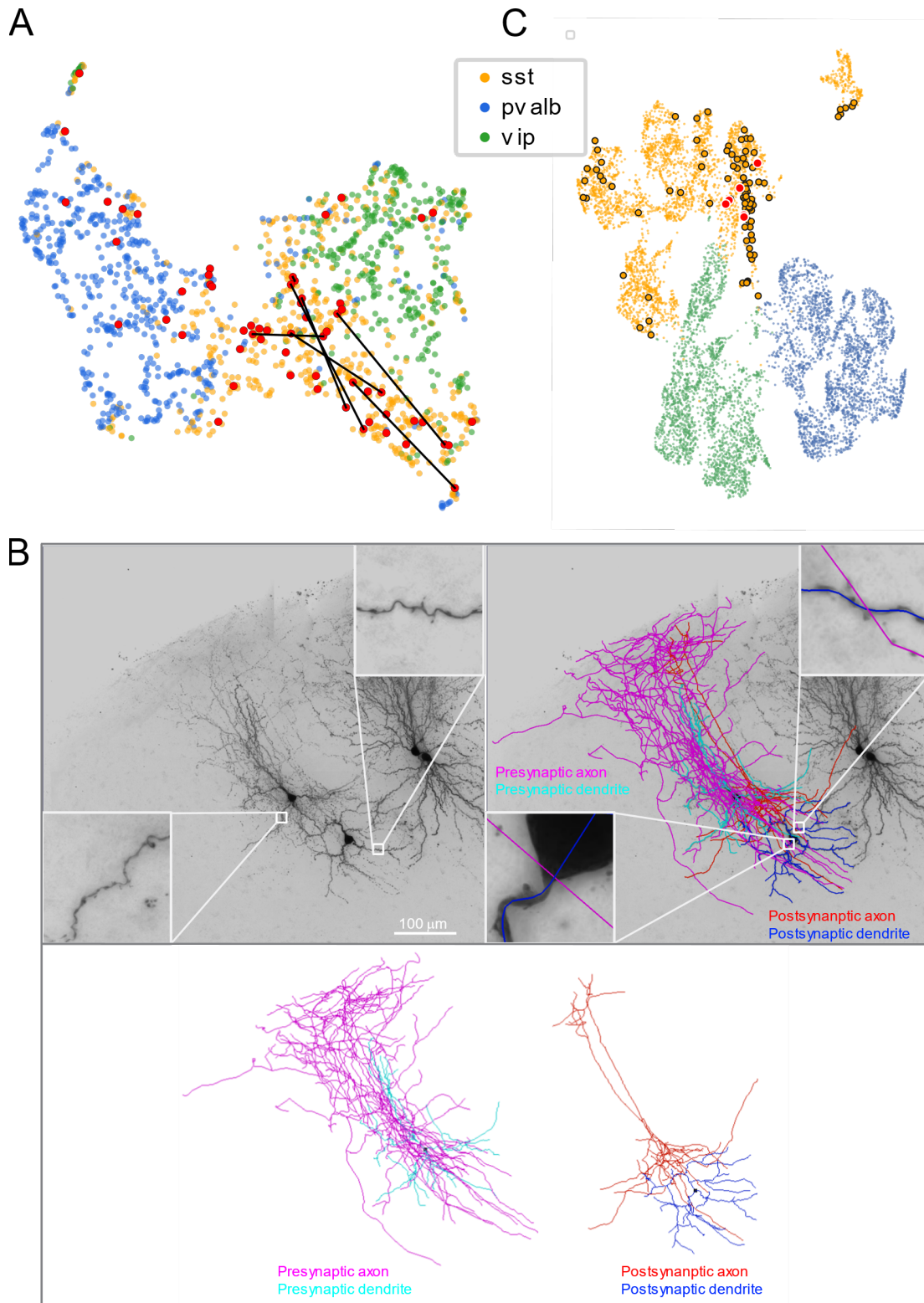


Fig. S3. Intrinsic uMap and morphologies of Sst recurrent connections. **A.** UMAP projection of electrophysiology feature space for all mouse inhibitory interneurons. Sst-cre/flp to Sst-cre/flp chemical synaptic connections (colored lines) are overlaid. Umap is color coded by the transgenic cell class. 8 out of 18 Sst to Sst connections had pre- and post-synaptic neurons that mapped with other Sst neurons and apart from Pvalb-cre/flp neurons. Only Sst to Sst connections that fall within the Sst island are indicated with a line. Sst-cre/flp cells that are part of a connection are indicated in red. **B.** Biocytin image of connected Sst-cre to Sst-cre connected cells with Sst-like morphologies (left). Insets show sparsely spiny dendrites for pre and post synaptic cell. Biocytin image with overlaid reconstructions (right). Insets show sites of close apposition between axon and dendrite of connected neurons. Reconstructions from C, shown independently (bottom). **C.** UMAP projection of IVSCC patchseq, FACS, and mSeq feature space of mouse inhibitory interneurons. Large dots in the Sst space highlight those from mSeq with cells from Sst→Sst connections further highlighted in red.

Fig S4

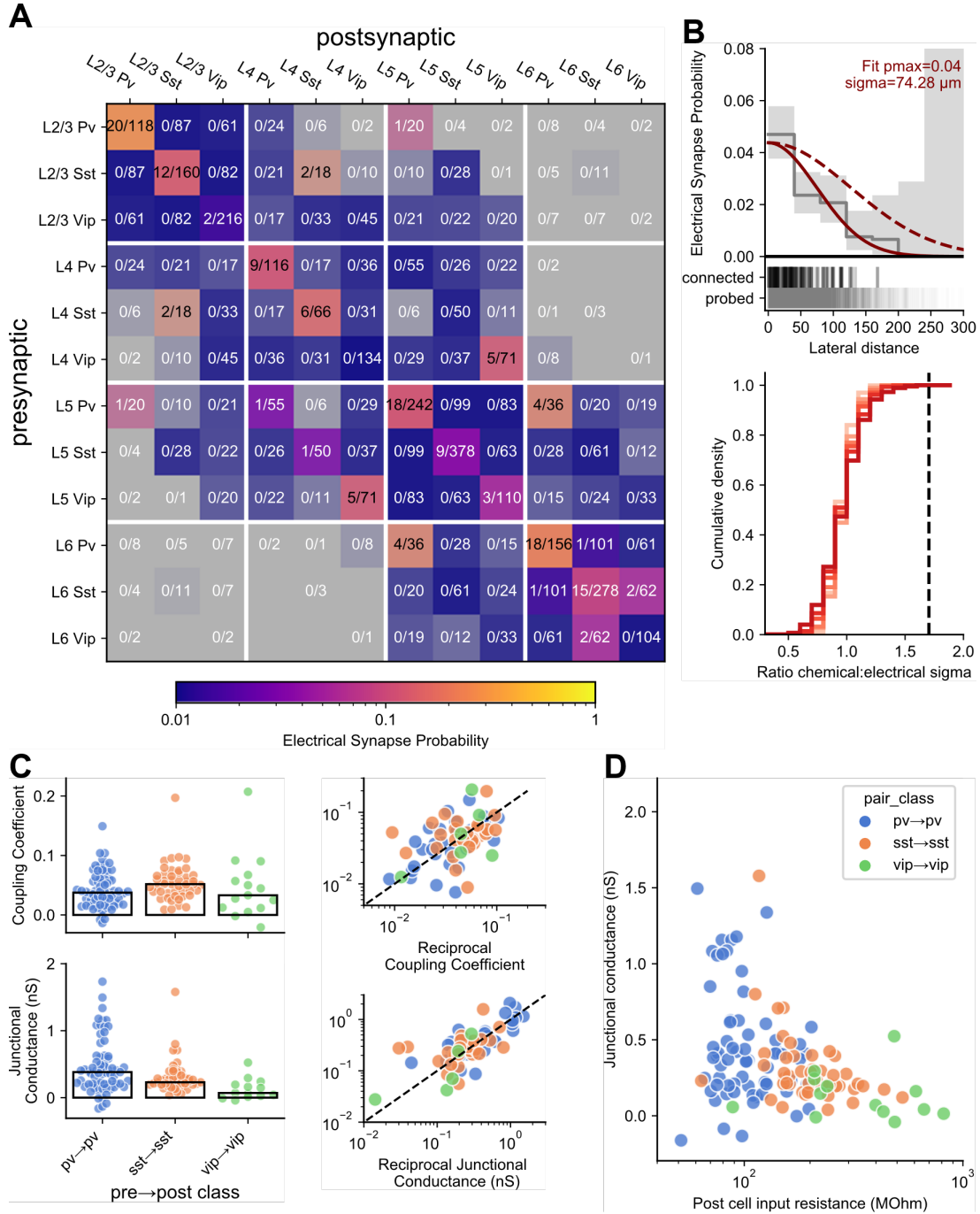


Fig. S4. Electrical Connections. **A.** Electrical connectivity matrix among inhibitory cells in each layer from mouse. **B.** (upper) Electrical connection probability as a function of lateral intersomatic distance with 95% confidence interval (grey line/shading) fit with a Gaussian (solid red line). Dotted red line shows Gaussian fit of chemical I→I connections (normalized to electrical p_{max}) for reference and to highlight shorter σ of electrical connections. (lower) Cumulative histogram of σ ratio comparing chemical and electrical connections. 1000 experiments were simulated in which the true σ for electrical and chemical connections was set to six evenly distributed values between 65 and 140 μm (light to dark red). We then measured the ratio of the Gaussian fit σ between chemical and electrical connections from those 1000 experiments which are plotted here as a cumulative histogram (a value of 1 indicates that the Gaussian profile of electrical and chemical connections has the same σ). The dotted vertical line denotes the measured σ ratio between chemical and electrical connections and sits beyond the 99th percentile for all simulations. **C.** Coupling coefficient (top) and junctional conductance (bottom) of recurrent I→I electrical connections. Left plots show a scatter where each dot is the value for a single unidirectional electrical connection and bars denote the median. Right plots show coupling coefficient and junctional conductance of each electrical connection vs its reciprocal connection (dotted line is unity line). **D.** Junctional conductance as a function of input resistance of the postsynaptic cell.

Fig. S5

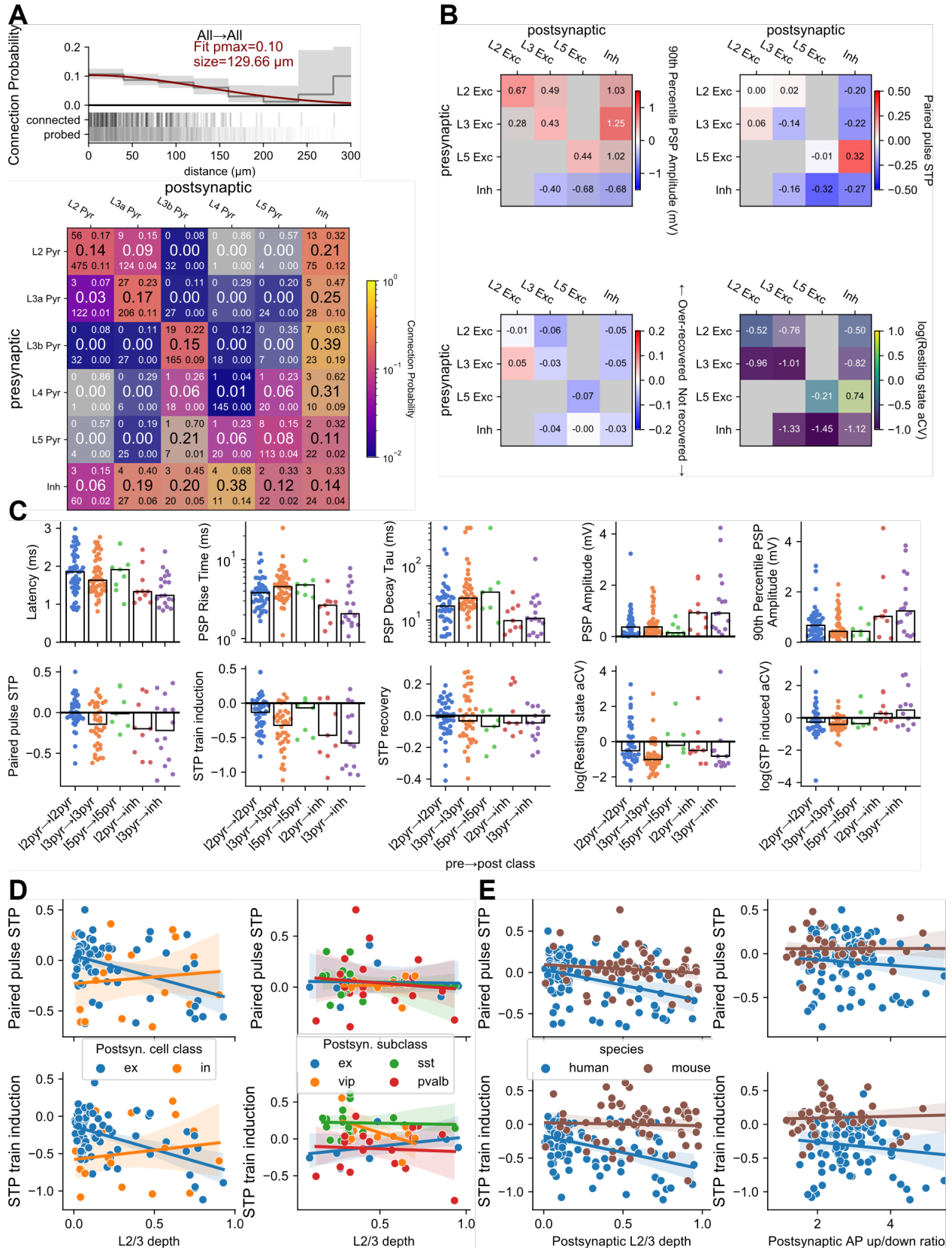


Fig. S5. Human Data. **A.** Gaussian fit of connection probability for all human connections. Connection probability as a function of lateral intersomatic distance was fit with a Gaussian (red line). Output parameters p_{max} and $size$ describe the max connection probability and sigma of the Gaussian. Grey line and area are 40 μm binned average connection probability and 95% confidence interval. Raster below shows distance distribution of connections probed (bottom) and found (top). Bottom panel shows connectivity matrix from Fig 5A with additional details quantified, as in Fig S2A (number tested/probed, left; lower/upper 95% CI bounds, right). **B.** Additional STP and variability metrics of human connections. Matrices are organized by layer for excitatory cells, with inhibitory cells grouped across layer. Each element is colorized by the grand average (text in each element) according to the colormap with the saturation scaled to the standard error. Two or more pairs were required to fill in an element. **C.** Summary plots for a range of PSP strength, timing, STP, and variability measurements. Each dot corresponds to the average response from one connection. Responses are shown for a subset of matrix elements with sufficient sampling. **D-E.** Additional correlates of STP variability in connections from L2/3 pyramidal cells. **D** shows dependence on postsynaptic cell class/subclass in human (left) and mouse (right). **E** shows decreased correlation with depth (left) and AP upstroke/downstroke ratio (right) when indexed to the postsynaptic cell.

Fig. S6

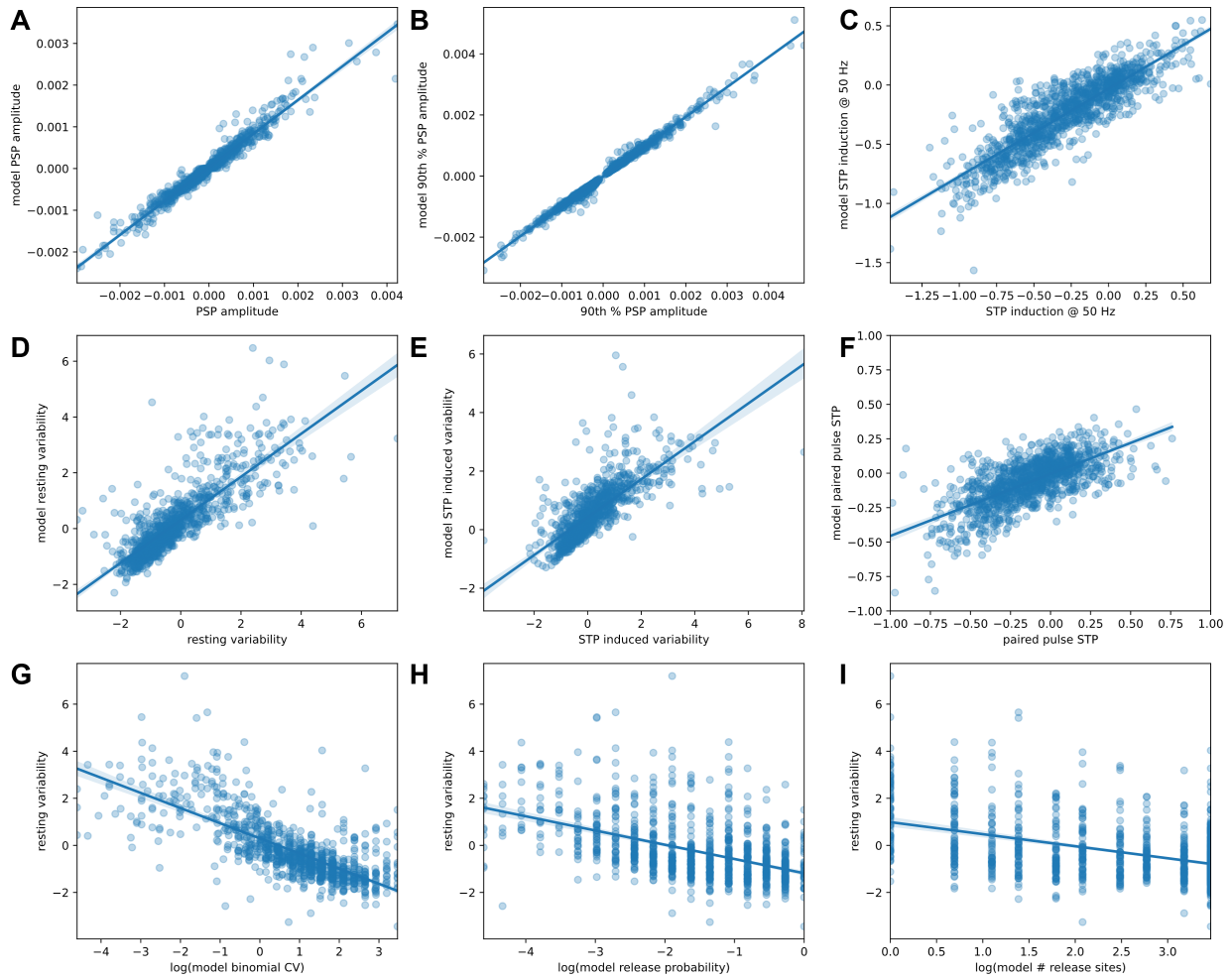


Fig. S6. Model output: Comparison between model behavior and measured connection features. For each connection, the maximum likelihood model parameters were used to simulate experimental data. Measurements were then performed on the simulated response amplitudes and compared to identical measurements from the recorded data. **A-B.** Measures of connection strength correlate strongly with model results. **C.** STP induced over the course of 8-pulse 50 Hz trains. **D.** Variability of resting-state PSP amplitudes. **E.** Variability of PSP amplitudes after STP induction. **F.** STP induced from first to second pulse in trains. **G.** Resting state variability correlates with the binomial CV derived from model parameters (the product of resting state release probability and number of release sites). **H-I.** Release probability is more strongly correlated with variability than number of release sites.

Fig. S7

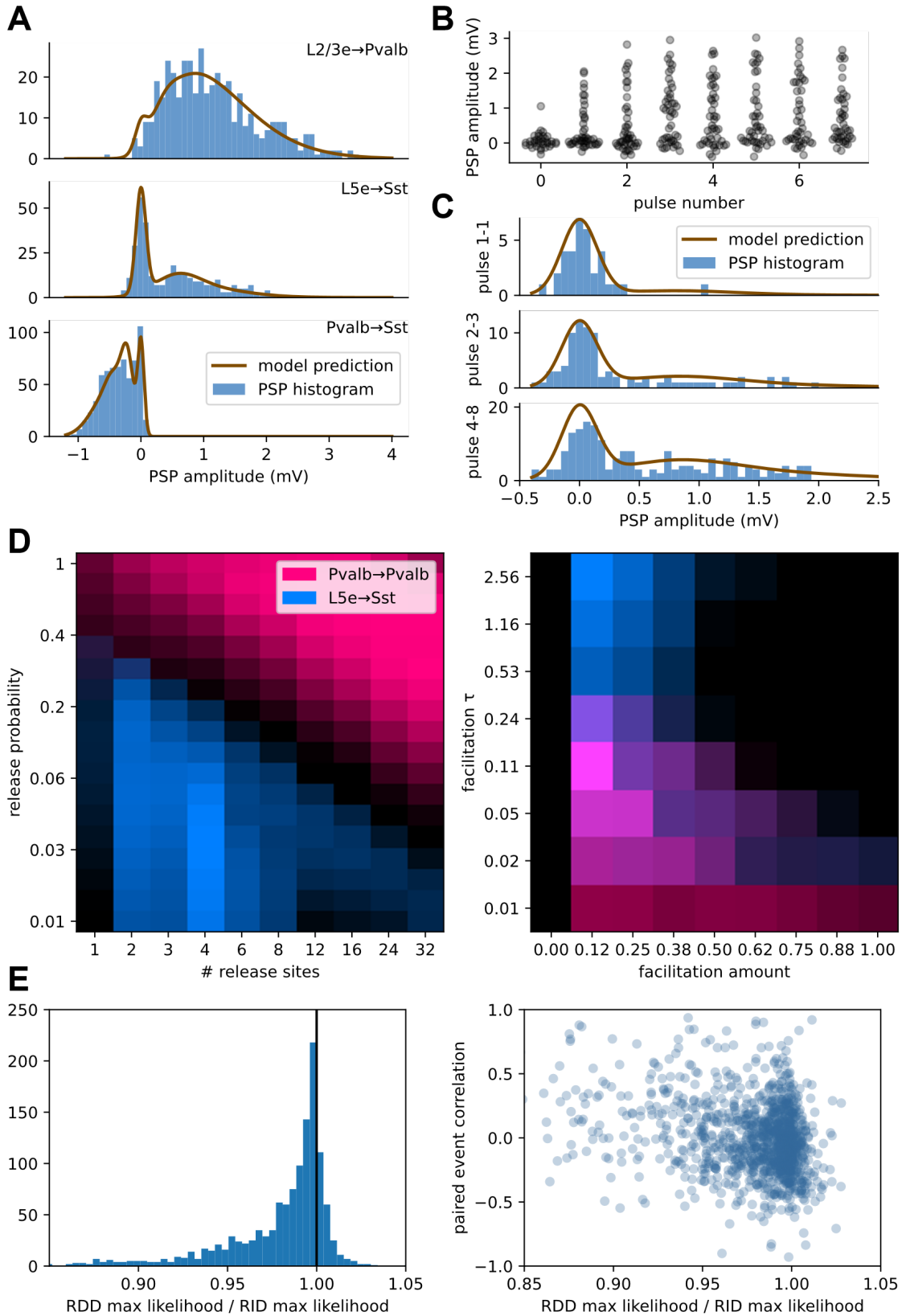


Fig. S7. Stochastic release model: A model of quantal release and short term plasticity. **A.** PSP amplitude histograms for three connections with the model's average predicted amplitude distribution overlaid. **B.** PSP amplitudes facilitating and reduction of synaptic failures across a 50 Hz spike train for the example L5e→Sst connection in (A). **C.** Histograms showing PSP amplitudes for the same connection with model distribution predictions overlaid, showing history-dependent adjustment in model state. **D.** Estimates of model likelihood (bright colors are higher likelihood) across a range of parameters for two connections. Each image is a maximum projection across all other axes in the model parameter space. **E.** Model results support release-independent depression mechanisms. Left: histogram of the ratios between release-dependent max likelihood and release-independent max likelihood, showing an overall preference for release-independent model parameters. Right: comparison of the same RDD/RID ratio to paired event correlations, with little overall effect. Release-dependent depression should result in negative paired event correlations.

Fig. S8

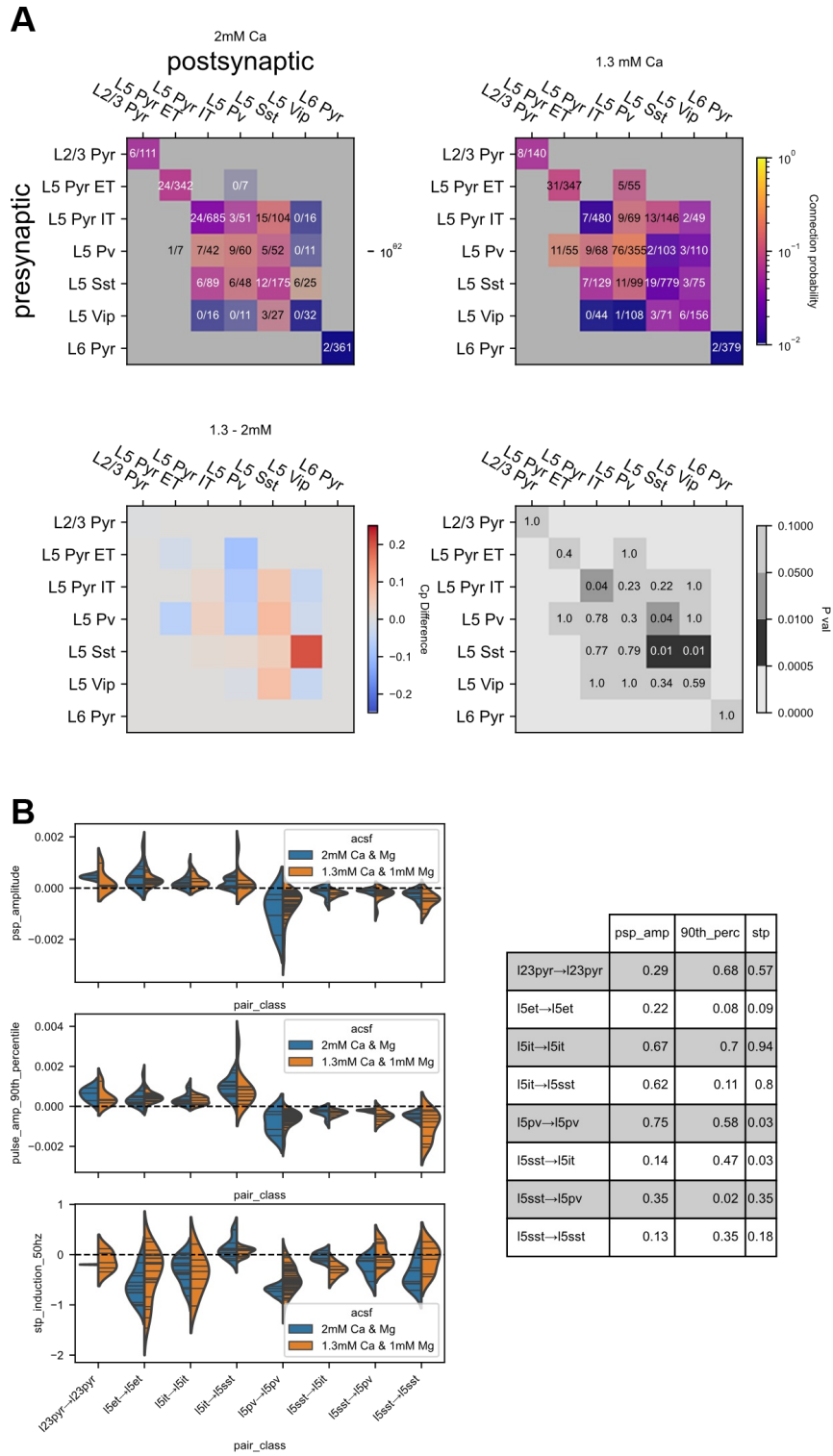


Fig. S8. External Calcium Concentration. **A.** Connectivity matrices of elements in mouse which were probed with both 2 mM external calcium and 1.3 mM external calcium in separate experiments (top row). The bottom left matrix is a difference of the 2 mM matrix from the 1.3 mM matrix. Red elements are those that showed higher connectivity in 1.3 mM calcium and blue elements those that showed higher connectivity in 2 mM calcium. The bottom right matrix shows uncorrected p-values from a Fisher-exact test for each element. **B.** Violin plot of measured PSP amplitude (resting state and 90th percentile) and induced STP of pairs for each element in 2 mM external calcium (blue) and 1.3 mM external calcium (orange). Measurements from individual pairs denoted by black lines within violin. Pairs/measurements are from different experiments, Kolmogorov-Smirnov p-values are shown in the table to the left for each element.

Fig. S9

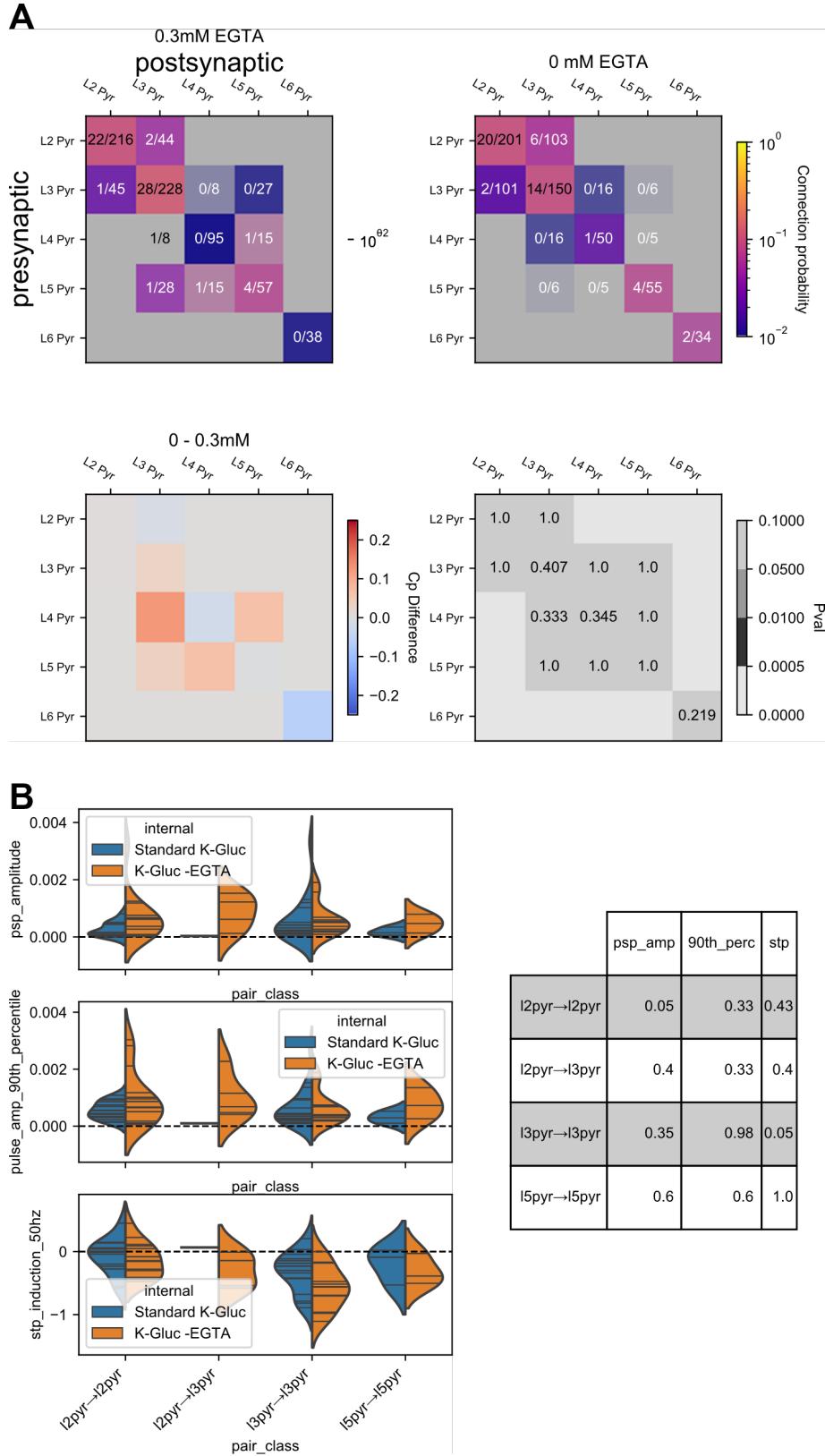


Fig. S9. Internal EGTA Concentration. A. Connectivity matrices of elements in human which were probed with both 0.3 mM internal EGTA and 0 mM internal EGTA in separate experiments (top row). The bottom left matrix is a difference of the 0.3 mM matrix from the 0 mM matrix. Red elements are those that showed higher connectivity in 0 mM calcium and blue elements those that showed higher connectivity in 0.3 mM calcium. The bottom right matrix shows uncorrected p-values from a Fisher-exact test for each element. **B.** Violin plot of measured PSP amplitude (resting state and 90th percentile) and induced STP of pairs for each element in 0.3 mM internal EGTA (blue) and 0 mM internal EGTA (orange). Measurements from individual pairs denoted by black lines within violin. Pairs/measurements are from different experiments, Kolmogorov-Smirnov p-values are shown in the table to the left for each element.

Fig. S10

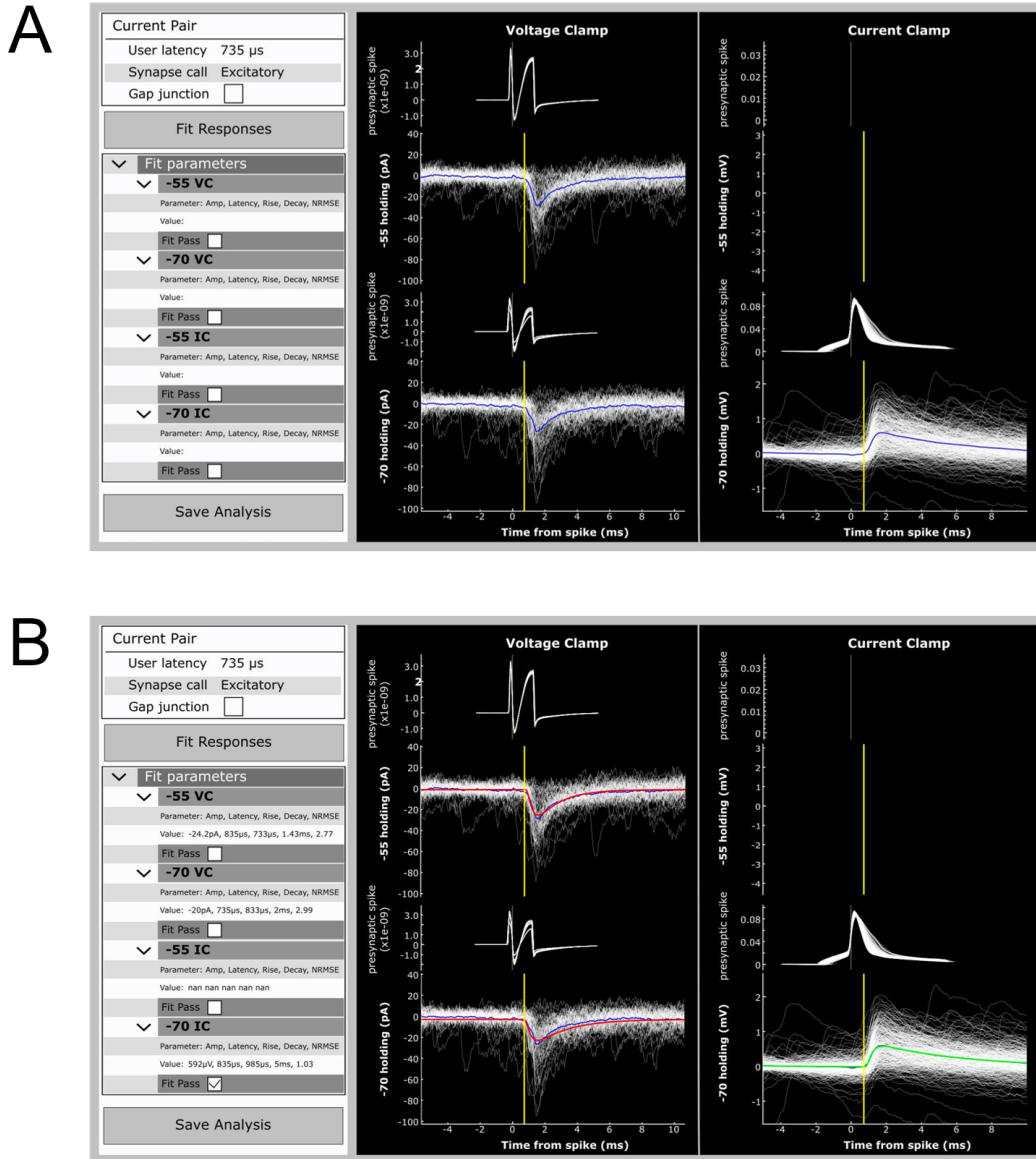


Fig. S10. Pair Analysis Tool. **A.** Pair analysis tool used to analyze connections. Postsynaptic responses and presynaptic spikes (white traces) from each pair were divided by clamp mode (voltage clamp on the left, current clamp on the right) and then again by baseline potential (depolarized potentials on the top, hyperpolarized potentials on the bottom). Responses from each quadrant were averaged (blue trace). If a connection was identified the user would select the type (excitatory or inhibitory) from the menu on the left and move the yellow line in any quadrant to the onset of the response (all lines are linked). The user would then select “Fit Response”. **B.** The fitting algorithm produces a fit of the PSC/P and plots in red (QC fail, NRMSE too high) or green (QC pass). Fit parameters for each quadrant are printed in the left menu. Users could shift the yellow line and refit to obtain a better fit. When the user was satisfied with the fit result or could not obtain a passing fit the analysis was saved.

Fig. S11

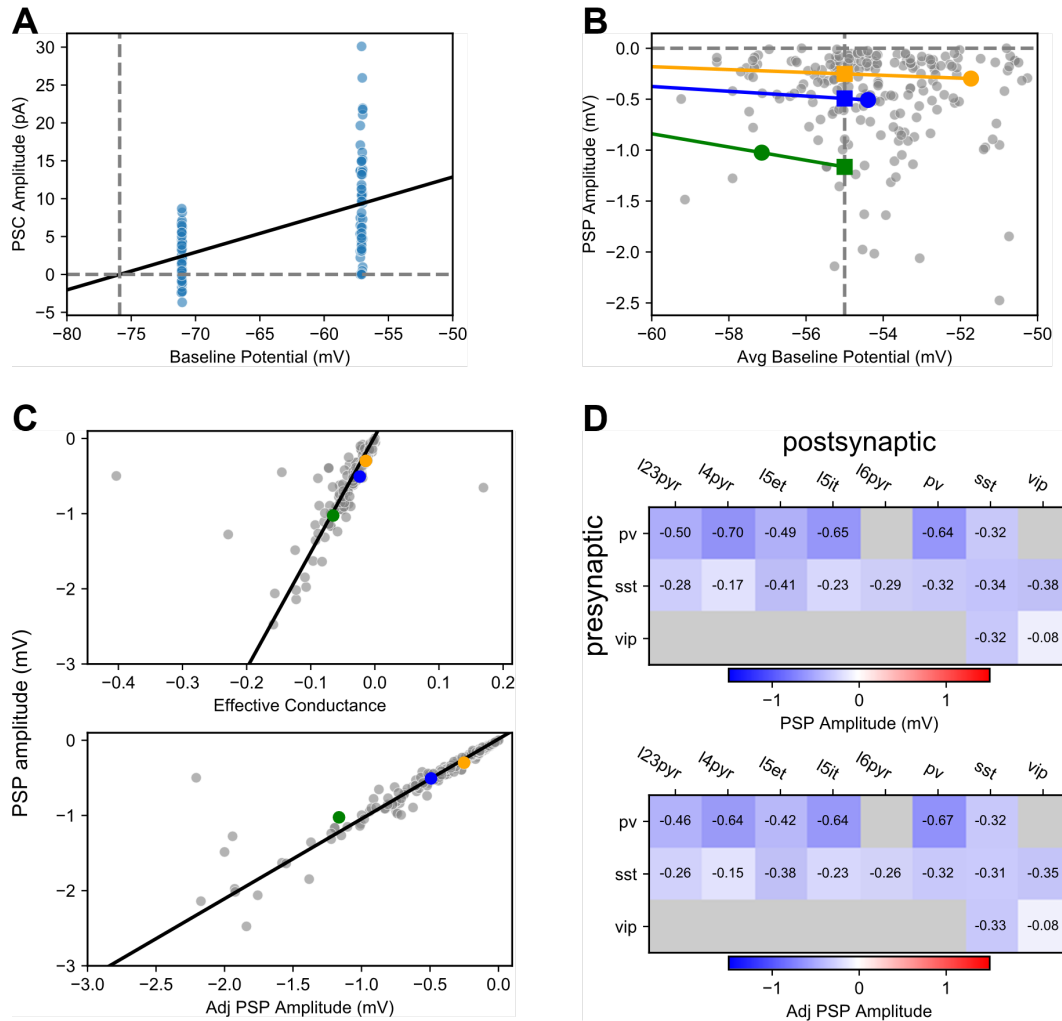


Fig. S11. Effective conductance of inhibitory connections. **A.** Voltage clamp responses from one pair at two different baseline potentials. Each dot represents the response evoked from one spike. The black line is a linear regression from which the reversal potential is determined as the y-intercept. The reversal potential for this connection was -75.9 mV (intersection of dotted lines). **B.** PSP amplitude as a function of average baseline potential for all inhibitory connections; each grey dot represents an individual connection. The blue dot is the same connection from (A). A line (blue line) was fit from the blue dot, through the reversal potential measured from (A). The slope of this line is the effective conductance and was used to calculate an adjusted PSP amplitude for this connection at -55 mV (vertical dotted line, blue square). Two other examples are shown for a pair where the postsynaptic cell was more depolarized (orange) or more hyperpolarized (green) than -55 mV **C.** Linear regression between effective conductance and resting state PSP amplitude (top, $R^2 = 0.42$) and between conductance adjusted PSP amplitude and resting state PSP amplitude (bottom, $R^2 = 0.88$). Each dot represents one connection. Colored dots correspond to those in (B) **D.** Matrices of resting state PSP amplitude (top) and adjusted resting state PSP amplitude (bottom) for inhibitory connections that had both measurements.

Fig. S12

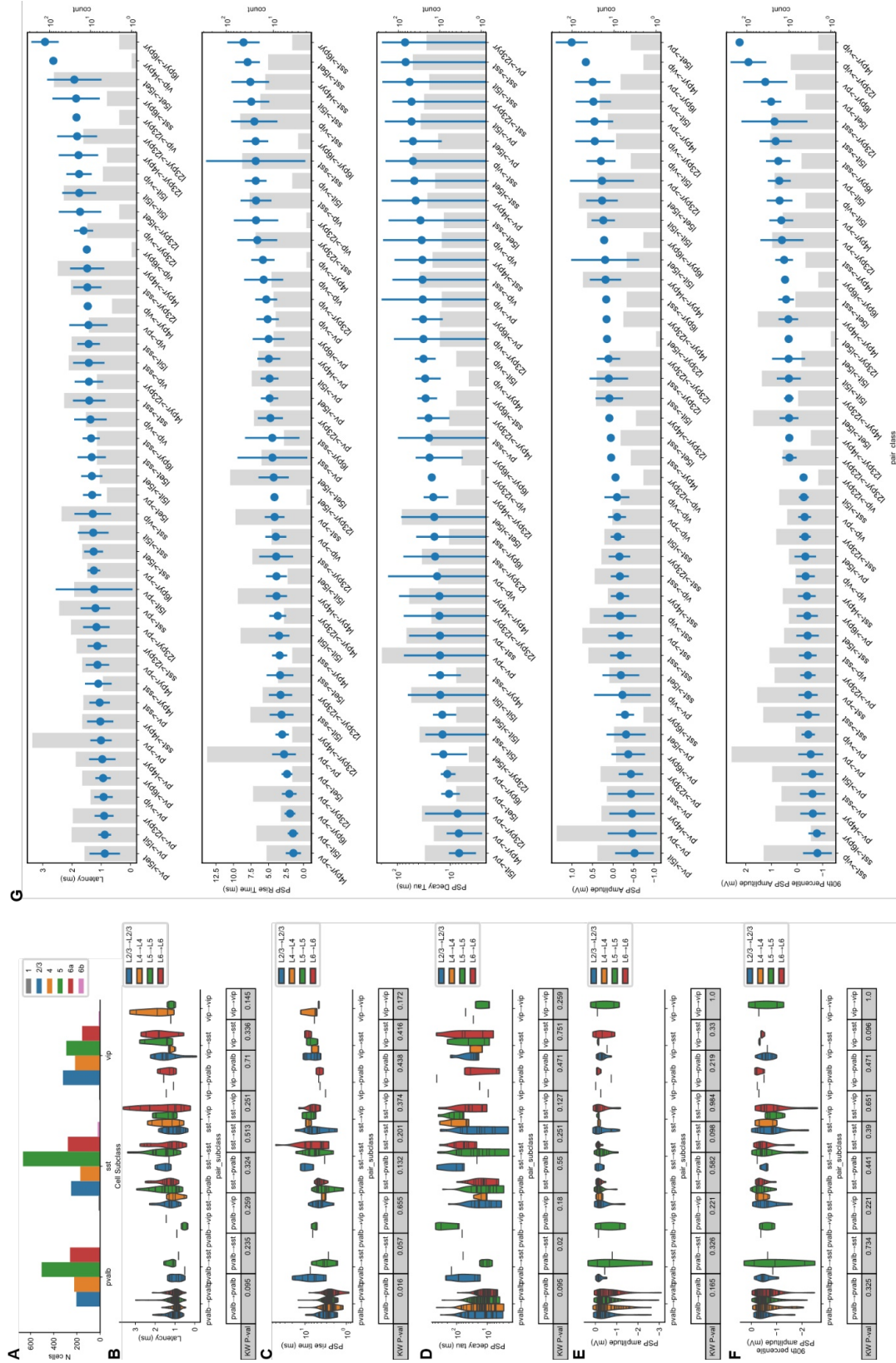


Fig. S12. Strength and Kinetics. **A.** The distribution of inhibitory cells according to layer. **B.** Latency of inhibitory \rightarrow inhibitory connections for all of the combinations among Pvalb, Sst, and Vip. For each connection element they are grouped by layer to estimate the variance of I \rightarrow I latency across layer. The table below shows the p-value from a Kruskal-Wallis (KW) test which suggests that within layer I \rightarrow I latency does not vary across layers. **C-F.** The same as B for PSP rise time (C), PSP decay tau (D), PSP resting state amplitude (E), and PSP 90th percentile amplitude (F). **G.** Average strength or kinetic measurement of each element in the 8 x 8 matrix from Figure 3 with standard deviation sorted from lowest to highest (blue dots, left axis) and number of pairs within each element shown in the grey bars (right axis).

Fig. S13

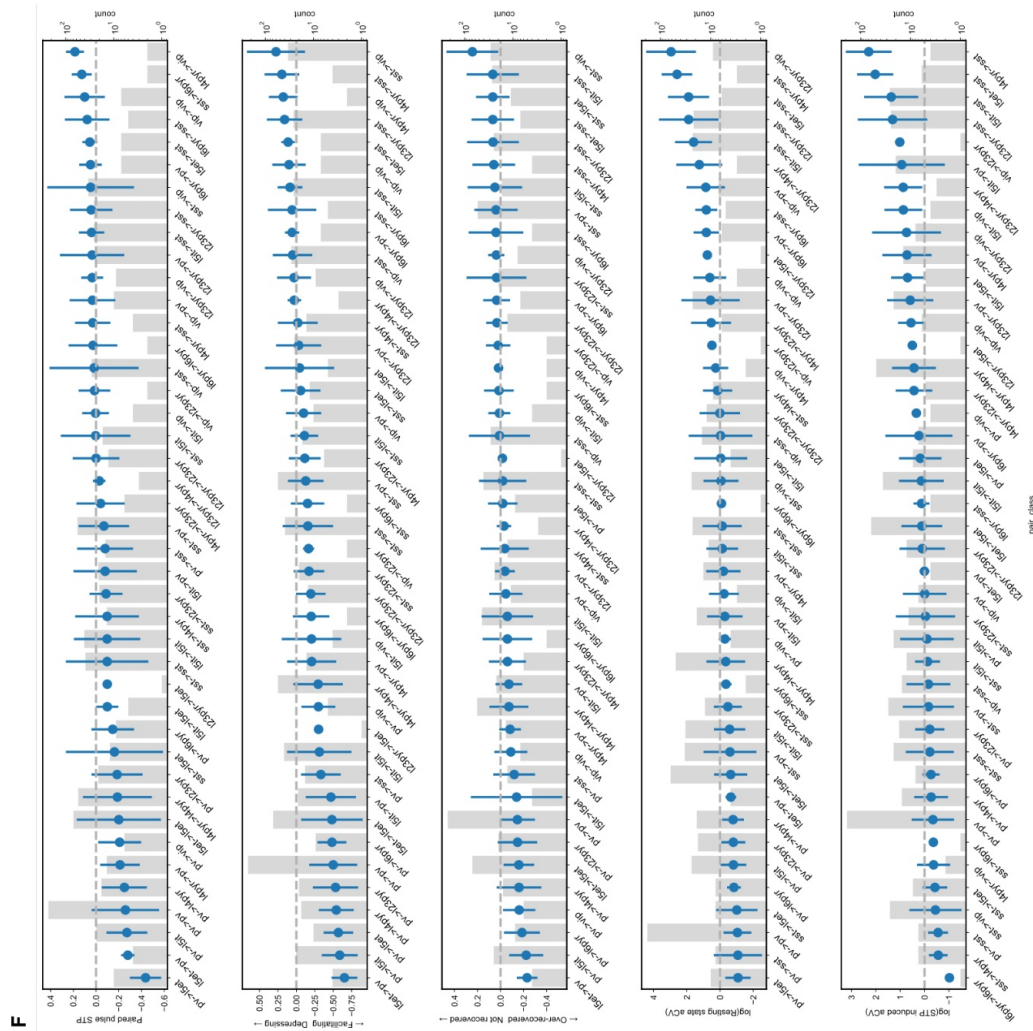
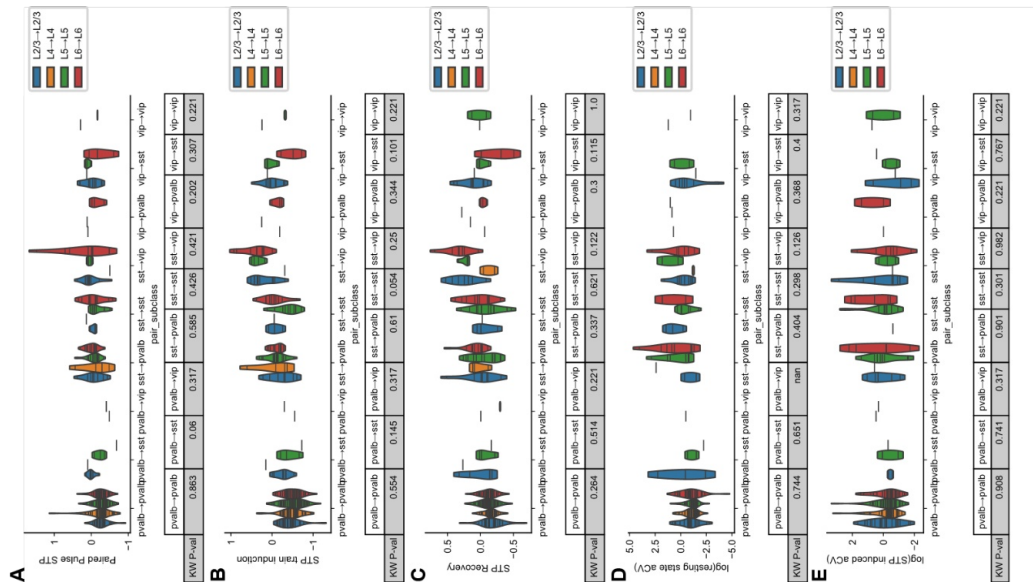


Fig. S13. Dynamics. **A.** Paired pulse ratio (stp_initial_50hz) of inhibitory → inhibitory connections for all of the combinations among Pvalb, Sst, and Vip. For each connection element they are grouped by layer to estimate the variance of I → I PPR across layer. The table below shows the p-value from a Kruskal-Wallis (KW) test which suggests that within layer I → I PPR does not vary across layers. **B-E.** The same as A for STP induction (B), STP recovery (C), resting state variability (D), and STP induced variability (E). **F.** Average dynamics measurement of each element in the 8 x 8 matrix from Figure 4 with standard deviation sorted from lowest to highest (blue dots, left axis) and number of pairs within each element shown in the grey bars (right axis).

Fig S14

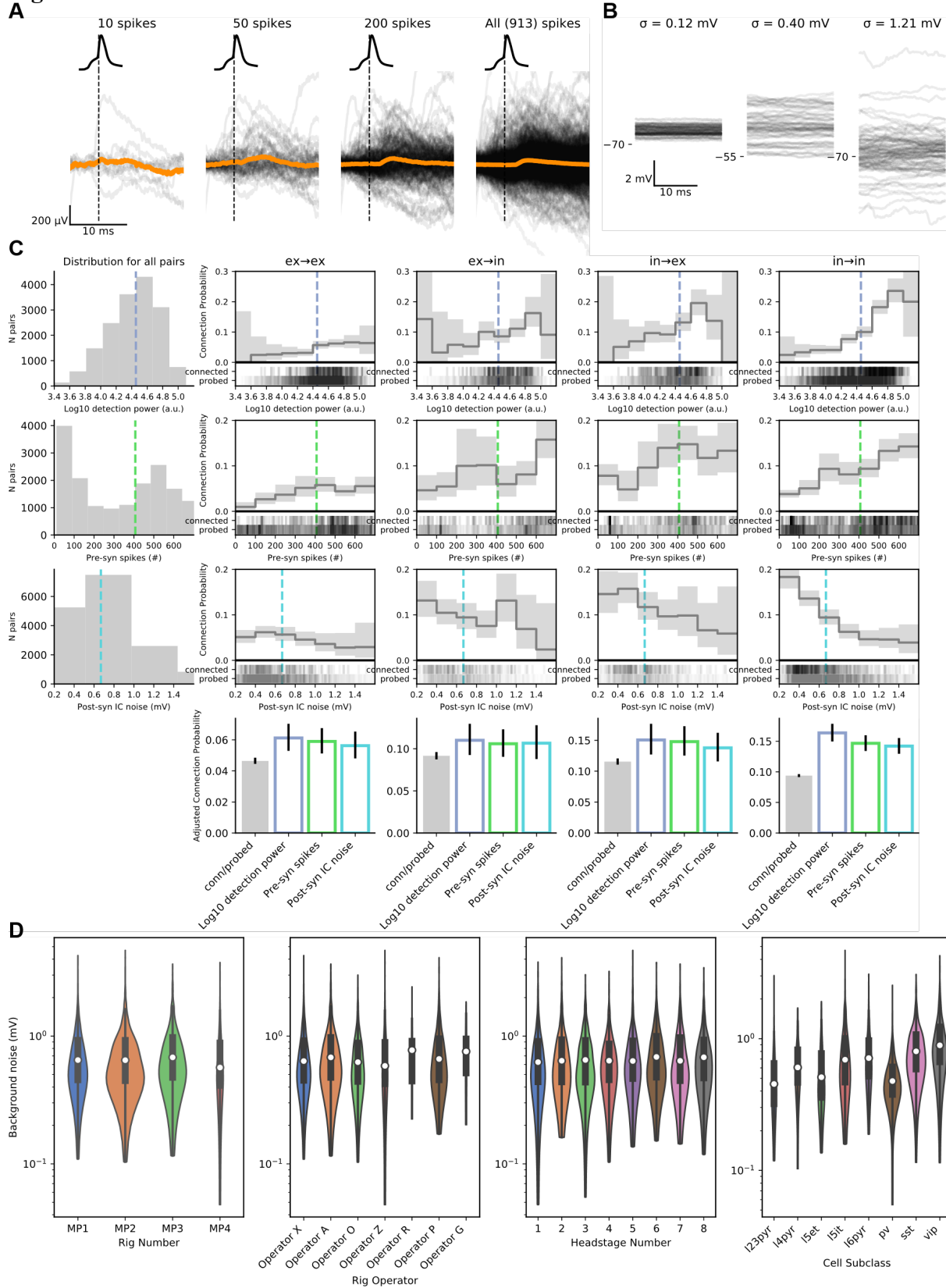


Fig S14. Detection power. **A.** Example pair shows how the number of presynaptic spikes delivered affects the ability to detect the synaptic response from the average (orange trace). Traces (black) are aligned to the steepest rise of the presynaptic action potential (dotted line). **B.** Three example cells highlighting low, medium, and high background noise. Background noise for each cell was calculated using the standard deviation of recording data from quiescent periods with no stimulation. 100 short chunks of quiescent data (chosen at random) are shown for three example cells. **C.** Plots follow those in Fig S2 for detection power, the number of presynaptic spikes, and background noise of postsynaptic cells. Bar plots in the bottom row show the results of data filtered above (detection power, presynaptic spikes) or below (background noise) their medians (dotted colored lines) and the effect on estimated p_{max} connection probability (following S2E). **D.** Distributions of background noise for individual cells as a function of (left to right): electrophysiology rig, rig operator, recording headstage (headstages were situated in a semicircle from 1-8), cell subclass. The width of the violin is scaled to the number of cells in each group. Inner box plot shows median (white circle) and IQR.

Table S1

Transgenic mouse line	Cre + reporter abbr.	FlpO + reporter abbrev.
Double Transgenic		
Pvalb-IRES-Cre;Ai14	Pvalb-TdTomato	
Sst-IRES-Cre;Ai14	Sst-TdTomato	
Nr5a1-Cre;Ai14	Nr5a1-TdTomato	
Tlx3-Cre_PL56;Ai14	Tlx3-TdTomato	
Sim1-Cre_KJ18;Ai14	Sim1-TdTomato	
Triple Transgenic		
Sst-IRES-Cre;Pvalb-T2A-FlpO;Ai193-hyg	Sst-EGFP	Pvalb-TdTomato
Vip-IRES-Cre;Sst-IRES-FlpO;Ai193-hyg	Vip-EGFP	Sst-TdTomato
Vip-IRES-Cre;Pvalb-T2A-FlpO;Ai193-hyg	Vip-EGFP	Pvalb-TdTomato
Sim1-Cre_KJ18;Sst-IRES-FlpO;Ai193-hyg	Sim1-EGFP	Sst-TdTomato
Sim1-Cre_KJ18;Vip-IRES-FlpO;Ai193-hyg	Sim1-EGFP	Vip-TdTomato
Sim1-Cre_KJ18;Pvalb-T2A-FlpO;Ai193-hyg	Sim1-EGFP	Pvalb-TdTomato
Quadruple Transgenic		
Sst-IRES-Cre;Ai140;Pvalb-T2A-FlpO;Ai65F	Sst-EGFP	Pvalb-TdTomato
Vip-IRES-Cre;Ai140;Sst-IRES-FlpO;Ai65F	Vip-EGFP	Sst-TdTomato
Vip-IRES-Cre;Ai140;Pvalb-T2A-FlpO;Ai65F	Vip-EGFP	Pvalb-TdTomato
Nr5a1-Cre;Ai140;Pvalb-T2A-FlpO;Ai65F	Nr5a1-EGFP	Pvalb-TdTomato
Nr5a1-Cre;Ai140;Sst-IRES-FlpO;Ai65F	Nr5a1-EGFP	Sst-TdTomato
Nr5a1-Cre;Ai140;Vip-IRES-FlpO;Ai65F	Nr5a1-EGFP	Vip-TdTomato
Pvalb-IRES-Cre;Ai140;Rorb-T2A-tTA2;Ai63	Pvalb-EGFP	Rorb-TdTomato
Tlx3-Cre_PL56;Ai140;Pvalb-T2A-FlpO;Ai65F	Tlx3-EGFP	Pvalb-TdTomato
Tlx3-Cre_PL56;Ai140;Sst-IRES-FlpO;Ai65F	Tlx3-EGFP	Sst-TdTomato
Tlx3-Cre_PL56;Ai140;Vip-IRES-FlpO;Ai65F	Tlx3-EGFP	Vip-TdTomato
Sim1-Cre_KJ18;Ai52;Pvalb-T2A-FlpO;Ai65F	Sim1-EGFP	Pvalb-TdTomato
Sim1-Cre_KJ18;Ai139;Sst-IRES-FlpO;Ai65F	Sim1-EGFP	Sst-TdTomato
Sim1-Cre_KJ18;Ai52;Vip-IRES-FlpO;Ai65F	Sim1-EGFP	Vip-TdTomato
Ntsr1-Cre_GN220;Ai140;Pvalb-T2A-FlpO;Ai65F	Ntsr1-EGFP	Pvalb-TdTomato
Ntsr1-Cre_GN220;Ai140;Sst-IRES-FlpO;Ai65F	Ntsr1-EGFP	Sst-TdTomato
Ntsr1-Cre_GN220;Ai140;Vip-IRES-FlpO;Ai65F	Ntsr1-EGFP	Vip-TdTomato
Double Transgenic + retroorbital AAV		
Tlx3-Cre_PL56;Ai193 + mscRE4-FlpO AAV PHPe.B	Tlx3-EGFP	mscRE4-TdTomato targets Layer 5 ET cells

Table S1. Transgenic Animals. List of transgenic animals used in experiments. Animals were derived from double, triple, or quadruple transgenics. In triple and quadruple transgenics, two subclasses were driven by either Cre or FlpO and expressed either TdTomato or EGFP. In one case we utilized a retroorbital AAV to label L5 ET cells together with L5 IT cells as it was not possible to construct this combination through a triple or quadruple transgenic.

Table S2

	presynaptic	excitatory	inhibitory	excitatory	inhibitory	excitatory	inhibitory	E subclasses	Pvalb,Sst,Vip	excitatory
postsynaptic	E/I	E/I	E,Pvalb,Sst,Vip	E,Pvalb,Sst,Vip	E	E	E subclasses	all	all	human,mouse
	classes	classes			subclasses	subclasses				E
test accuracy	0.83	0.73	0.72	0.57	0.42	0.30	0.39	0.74	0.76	0.76
shuffled accuracy	0.53	0.70	0.47	0.47	0.36	0.26	0.25	0.56	0.56	0.56
accuracy gain	0.64	0.09	0.47	0.19	0.09	0.05	0.19	0.41	0.45	0.45
mini_amplitude	0.47	0.00	0.34	-0.01	0.10	0.01	0.19	0.00	0.03	0.03
variability_second_pulse_50hz	0.25	0.00	0.23	-0.00	-0.01	0.01	0.03	0.22	0.21	0.21
stp_induction_50hz	0.27	0.00	0.16	0.07	-0.02	-0.03	0.10	0.32	0.00	0.00
variability_resting_state	0.32	0.00	0.24	-0.01	-0.01	0.00	0.05	0.20	0.02	0.02
variability_change_induction_50hz	0.26	-0.01	0.18	0.04	0.00	0.00	0.07	0.23	-0.00	-0.00
paired_pulse_ratio_50hz	0.24	0.00	0.18	0.00	0.01	-0.06	0.03	0.20	0.15	0.15
stp_recovery_single_250ms	-0.06	0.00	0.04	0.02	-0.01	-0.03	0.13	0.34	0.26	0.26
variability_stp_induced_state_50hz	0.26	0.00	0.11	-0.00	-0.02	0.01	0.03	0.06	0.21	0.21
quanta_per_spike	0.30	0.00	0.23	-0.01	0.07	-0.01	0.08	0.00	-0.02	-0.02
stp_recovery_250ms	0.06	0.00	0.11	0.04	-0.02	-0.07	0.06	0.32	0.09	0.09
pulse_amp_90th_percentile	0.19	0.00	0.05	0.00	0.03	0.04	0.09	0.00	0.08	0.08
facilitation_tau	0.00	0.00	0.00	-0.02	0.01	-0.00	0.01	0.20	0.26	0.26
variability_change_initial_50hz	0.18	0.00	0.10	0.03	0.01	-0.04	0.07	0.10	-0.01	-0.01
base_release_probability	0.26	0.00	0.13	0.00	-0.01	-0.02	0.04	0.02	-0.01	-0.01
measurement_stdev	0.08	0.04	-0.01	0.05	-0.01	0.03	-0.00	0.07	-0.02	-0.02
facilitation_amount	0.18	0.00	0.00	-0.00	-0.00	0.02	-0.02	0.00	0.00	0.00
strength	0.01	0.00	-0.01	0.00	0.01	-0.01	-0.03	0.19	0.00	0.00
stp_initial_50hz	-0.01	0.00	-0.09	-0.02	0.02	0.01	0.15	0.14	-0.04	-0.04
depression_tau	0.00	0.00	-0.01	0.00	0.01	0.00	0.10	0.00	0.01	0.01
release_dependence_ratio	0.17	0.00	-0.05	-0.00	0.00	-0.00	0.03	-0.04	-0.03	-0.03
mini_amplitude_cv	0.17	0.00	-0.06	-0.00	0.01	0.03	-0.08	0.00	0.00	0.00
n_release_sites	0.02	0.00	0.06	-0.01	-0.04	0.02	0.01	0.00	0.00	0.00
noise_amp_90th_percentile	-0.00	0.00	0.00	-0.00	-0.00	0.00	-0.00	0.00	-0.00	-0.00
depression_amount	0.02	0.00	0.00	0.00	0.02	-0.05	0.00	0.00	0.01	0.01
sites_pr_ratio	0.03	0.00	-0.02	0.00	-0.01	-0.00	-0.02	0.00	0.00	0.00

Table S2. Connection features related to subclass. Summary of 9 different classifiers used to determine the relationship between connection features and pre- or postsynaptic cell subclass. The first two rows indicate the classifications that were used. Rows 3-5 describe the accuracy of the classifier after fitting, where accuracy gain is the percent increase in test accuracy over shuffled (see Methods). The remaining rows show the accuracy gain in classification using only one feature at a time. Excitatory subclasses included L2/3, L4, L5ET, L5IT, and L6CT.

Table S3

Component	ACSF.I	ACSF.IV	ACSF.V	ACSF.VII	ACSF.IX
Calcium Chloride, dihydrate	0.5 mM	2 mM	1.8 mM	0.5 mM	1.3/2.0 mM
D-Glucose (Dextrose)	25 mM	25 mM	0	25 mM	25 mM
HCl	98 mM	0	0	92 mM	0
HEPES	20 mM	20 mM	5 mM	20 mM	0
Magnesium Chloride	0	0	1.0 mM	0	0
Magnesium Sulfate	10 mM	2 mM	0	10 mM	1.0/2.0 mM
Monosodium Phosphate	1.25 mM	1.25 mM	0	1.2 mM	1.2 mM
Myo inositol	3 mM	3 mM	0	0	0
N-acetylcysteine	12 mM	12.3 mM	0	0	0
N-methyl-d-glucamine	96 mM	0	0	92 mM	0
Potassium Chloride	2.5 mM	2.5 mM	5.4 mM	2.5 mM	3mM
Sodium Bicarbonate	25 mM	25 mM	0	30 mM	18 mM
Sodium Chloride	0	94 mM	135 mM	0	126 mM
Sodium L-Ascorbate	5 mM	5 mM	0	5 mM	0.16 mM
Sodium Pyruvate	3 mM	3 mM	0	3 mM	0
Taurine	0.01 mM	0.01 mM	0	0	0
Thiourea	2 mM	2 mM	0	2 mM	0

Table S3. ACSF Recipes. Concentrations of each component in ACSF recipes utilized in different stages of our experiments, slice, holding, recording, etc. See Methods for more information on when each ACSF was used.

Table S4

QC Metric	Analysis level of data being evaluated	Voltage Clamp	Current Clamp
Holding current	Postsynaptic stimulus trial	± 800 pA	± 800 pA
Holding potential	Postsynaptic stimulus trial		-50 to -85 mV
Baseline noise	Postsynaptic stimulus trial	< 200 pA	< 5 mV
Presynaptic spike detected	Presynaptic recording in response to 1 stimulus pulse	✓	✓
Extra spikes	Presynaptic recording in response to 1 stimulus pulse	None within ± 8 ms	None within ± 8 ms
Standard deviation of postsynaptic response This checks for a relatively stable baseline	Postsynaptic recording in response to 1 stimulus pulse	< 15 pA	< 1.5 mV
Max postsynaptic amplitude This checks for artifacts in the response	Postsynaptic recording in response to 1 stimulus pulse	< 500 pA	< 10 mV
Max postsynaptic potential	Postsynaptic recording in response to 1 stimulus pulse		-40 mV
Excitatory connections	Postsynaptic recording in response to 1 presynaptic spike	Membrane potential between -50 and -80 mV	
Inhibitory connections	Postsynaptic recording in response to 1 presynaptic spike	Membrane potential between -50 and -60 mV	

Table S4. Quality Control. Quality control stages for data processing.

Table S5

Morphology annotation	Description
<i>Dendrite type</i>	
NEI (Not Enough Information)	Either no biocytin filled cell or poor health precludes definition of dendrite type
Aspiny	No visible spines, non-pyramidal morphology
Sparsely spiny	Visible spines, non-pyramidal morphology
Spiny	Visible spines, pyramidal or stellate morphology
<i>Axon</i>	
Truncation	Obvious cut axon or retraction bulb near surface of the slice that measured $\leq 100 \mu\text{m}$
Borderline	Axon measured between 100-200 μm
Intact	Traceable axon measured $> 200 \mu\text{m}$
Unclear	Axon untraceable but not obviously truncated, likely due to poor health or biocytin fill
Truncation distance	Length of axon measured as the straight line distance from origin to end. Only measured in "truncated" or "borderline" axons
<i>Apical dendrite</i>	
Truncated	Does not reach Layer 1
Intact	Reaches Layer 1
Truncation distance	Length of largest apical branch measured as the straight line distance from soma to end of dendrite. Only measured in "truncated" dendrites

Table S5. Morphology Annotations. Morphological annotations assigned to recorded cells filled with biocytin and imaged at 63x resolution.